



HAL
open science

Diagenetic alteration of natural Fe-Ti oxides identified by energy dispersive spectroscopy and low-temperature magnetic remanence and hysteresis measurements

Melanie Dillon, Christine Franke

► **To cite this version:**

Melanie Dillon, Christine Franke. Diagenetic alteration of natural Fe-Ti oxides identified by energy dispersive spectroscopy and low-temperature magnetic remanence and hysteresis measurements. *Physics of the Earth and Planetary Interiors*, 2008, 172 (3-4), pp.141. 10.1016/j.pepi.2008.08.003 . hal-00532173

HAL Id: hal-00532173

<https://hal.science/hal-00532173>

Submitted on 4 Nov 2010

HAL is a multi-disciplinary open access archive for the deposit and dissemination of scientific research documents, whether they are published or not. The documents may come from teaching and research institutions in France or abroad, or from public or private research centers.

L'archive ouverte pluridisciplinaire **HAL**, est destinée au dépôt et à la diffusion de documents scientifiques de niveau recherche, publiés ou non, émanant des établissements d'enseignement et de recherche français ou étrangers, des laboratoires publics ou privés.

Accepted Manuscript

Title: Diagenetic alteration of natural Fe-Ti oxides identified by energy dispersive spectroscopy and low-temperature magnetic remanence and hysteresis measurements

Authors: Melanie Dillon, Christine Franke

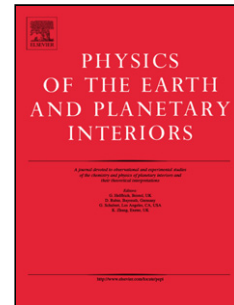
PII: S0031-9201(08)00224-0
DOI: doi:10.1016/j.pepi.2008.08.003
Reference: PEPI 5043

To appear in: *Physics of the Earth and Planetary Interiors*

Received date: 20-12-2007
Revised date: 24-7-2008
Accepted date: 6-8-2008

Please cite this article as: Dillon, M., Franke, C., Diagenetic alteration of natural Fe-Ti oxides identified by energy dispersive spectroscopy and low-temperature magnetic remanence and hysteresis measurements, *Physics of the Earth and Planetary Interiors* (2007), doi:10.1016/j.pepi.2008.08.003

This is a PDF file of an unedited manuscript that has been accepted for publication. As a service to our customers we are providing this early version of the manuscript. The manuscript will undergo copyediting, typesetting, and review of the resulting proof before it is published in its final form. Please note that during the production process errors may be discovered which could affect the content, and all legal disclaimers that apply to the journal pertain.



1 **Diagenetic alteration of natural Fe-Ti oxides identified by energy dispersive**
2 **spectroscopy and low-temperature magnetic remanence and hysteresis measurements**

3 Melanie Dillon*¹ and Christine Franke^{1,2}

4 ¹ Department of Geosciences, University of Bremen, P.O. Box 330 440, 28334 Bremen,
5 Germany

6 ² Laboratoire des Sciences du Climat et de l'Environnement, CEA-CNRS-UVSQ, Campus du
7 CNRS, Bat. 12, Avenue de la Terrasse, 91190 Gif-sur-Yvette Cedex, France

8 * corresponding author: e-mail: mdillon@uni-bremen.de; fax: +49-421-218-7008

9
10 **Abstract**

11 Low-temperature (LT) magnetic remanence and hysteresis measurements, in the range 300 to
12 5 K, were combined with energy dispersive spectroscopy (EDS) in order to characterize the
13 magnetic inventory of strongly diagenetically altered sediments originating from the Niger
14 deep-sea fan. We demonstrate the possibility of distinguishing between different
15 compositions of members of the magnetite-ulvöspinel and ilmenite-hematite solid solution
16 series on a set of five representative samples, two from the upper suboxic and three from the
17 lower sulfidic anoxic zone. Highly sensitive LT magnetic measurements were performed on
18 magnetic extracts resulting in large differences in the magnetic behaviour between samples
19 from the different layers. This emphasizes that both Fe-Ti oxide phases occur in different
20 proportions in the two geochemical environments.

21 Most prominent are variations in the coercivity sensitive parameter coercive field (B_C). At
22 room-temperature (RT) hysteresis loops for all extracts are narrow and yield low coercivities
23 (6 - 13 mT). With decreasing temperature the loops become more pronounced and wider. At
24 5 K an approximately 5-fold increase in B_C for the suboxic samples contrasts a 20- to 25-fold

25 increase for the samples from the anoxic zone. We demonstrate that this distinct increase in
26 B_C at LT corresponds to the increasing proportion of the Ti-rich hemoilmenite phase, while
27 Fe-rich (titano-)magnetite dominates the magnetic signal at RT. This trend is also seen in the
28 room-temperature saturation isothermal remanent magnetization (RT-SIRM) cycles: suboxic
29 samples show remanence curves dominated by Fe-rich mineral phases while anoxic samples
30 display curves clearly dominated by Ti-rich particles.

31 We show that the EDS intensity ratios of the characteristic Fe K_α and Ti K_α lines of the Fe-
32 Ti-oxides may be used to differentiate between members of the magnetite-ulvöspinel and
33 ilmenite-hematite solid solution series. Furthermore it is possible to calculate an approximate
34 composition for each grain if the intensity ratios of natural particles are linked to well known
35 standards. Thus, element spectra with high Fe/Ti intensity ratios were found to be rather
36 typical of titanomagnetite while low Fe/Ti ratios are indicative of hemoilmenite.

37 The EDS analyses confirm the LT magnetic results, Fe-rich magnetic phases dominate in
38 the upper suboxic environment whereas Ti-rich magnetic phases comprise the majority of
39 particles in the lower anoxic domain: The mineral assemblage of the upper suboxic
40 environments is composed of magnetite (~19 %), titanomagnetite (~62 %), hemoilmenite
41 (~17 %) and ~2 % other particles. In the lower anoxic sediments, reductive diagenetic
42 alteration has resulted in more extensive depletion of the (titano-)magnetite phase, resulting in
43 a relative enrichment of the hemoilmenite phase (~66 %). In these strongly anoxic sediments
44 stoichiometric magnetite is barely preserved and only ~5 % titanomagnetite was detected. The
45 remaining ~28 % comprises Ti-rich particles such as pseudobrookite or rutile.

46

47 **Keywords:** magnetic Fe-Ti oxides, energy dispersive spectroscopy (EDS), marine sediments,
48 scanning electron microscopy (SEM), low-temperature magnetism, early diagenesis

49 **Introduction**

50 A detailed rock magnetic study of diagenetically altered sediments from the Niger deep-sea
51 fan (GeoB 4901) was reported recently by Dillon & Bleil (2006). Room-temperature
52 hysteresis, IRM, ARM, high- and low-temperature data were combined to provide a
53 comprehensive interpretation of the magnetic assemblage and its modification by a variety of
54 diagenetic processes. The authors suggested that the vast majority of the magnetic assemblage
55 reaching the core location was composed of eroded volcanic material originating from the
56 Cameroon Volcanic Line. The volcanic assemblage was considered to be of variable
57 composition, containing Ti-poor and Ti-rich titanomagnetites and
58 ilmenohematites / hemoilmenites (Herrero-Bervera et al., 2004, Ubangoh et al., 2005).

59 At gravity core location GeoB 4901 (02°40.7'N / 06°43.2'E, 2184 m water depth, Schulz
60 et al., 1998; Fig. 1) the degradation of organic matter results in a specific redox zonation of
61 the sediment column, with only the upper 10 cm being oxic. Suboxic conditions are
62 characterized by dissolved manganese in the pore water and are established down to 12.50 m.
63 Anoxic conditions prevail below this level where anaerobic oxidation of methane results in
64 free H₂S in the pore water (Heuer, 2003). In this distinct redox zonation the magnetic iron
65 oxide mineral inventory undergoes a two-stage diagenetic alteration. The modern iron redox
66 boundary (~2.95 m) is characterized by a drastic decline in magnetic mineral content, a
67 coarsening of the grain size spectrum, and a reduction in coercivity at room-temperature. Such
68 reductive diagenesis in the suboxic zone is a common and frequently studied phenomenon in
69 organic rich marine sediments (e.g. Karlin and Levi, 1985; Canfield and Berner, 1987). Below
70 the second diagenetic horizon, the suboxic / sulfidic anoxic transition (~12.50 m), a further
71 but less pronounced decrease in magnetic concentration and grain size occurs. The
72 contribution of finer magnetic particles and the proportion of higher coercive magnetic
73 constituents substantially increase in the anoxic environment (Dillon and Bleil, 2006).

74 Diagenetic alteration of the primary detrital magnetic mineral inventory was found to be
75 dependent on both particle size and Ti-content, with the smallest particles dissolving first and
76 the Ti-rich component being more resistant to the reducing conditions. Possible candidates for
77 the preserved grains are titanomagnetite ($\text{Fe}_{3-x}\text{Ti}_x\text{O}_4$) and hemoilmenite ($\text{Fe}_{2-y}\text{Ti}_y\text{O}_3$) with
78 compositions of $x > 0.75$ and $y > 0.75$, respectively. Both mineral phases with Ti-contents
79 ≥ 0.75 are paramagnetic at ambient temperatures and exhibit high magnetic stabilities at low-
80 temperature (Bozorth et al., 1957; Schmidbauer and Readman, 1982; Ishikawa et al., 1985).
81 More recent work by Burton et al. (2008) states that this is actually the case for hemoilmenite
82 compositions of $y \geq 0.8$. Nevertheless, a definite distinction between the two mineral phases
83 remains unresolved. Titanomagnetites with such compositions are rather uncommon as
84 natural compounds. Therefore it appears more conceivable that Fe-Ti oxides of $y > 0.75$
85 constitutes hemoilmenite. The role of members of the ilmenite-hematite solid solution series
86 in a magnetic mineral assemblage is often disregarded, although these particles exist in a large
87 range of compositions and are frequent constituents of many types of rocks. However, the
88 presence of (titano-)magnetite usually masks the signature of the magnetic members of the
89 ilmenite-hematite solid solution series when both are present in a sample because the
90 saturation moment of magnetite is at least three times greater than that of e.g. hemoilmenite
91 ($y = 0.63$) at room temperature (Nord and Lawson, 1989). For the sake of clarity in
92 nomenclature we will use the term 'hemoilmenite' for compositions of $y \geq 0.5$ and the term
93 'ilmnohematite' for mineral phases with $y < 0.5$. Detailed compositions are expressed using
94 the definitions of Nord and Lawson, (1989), e.g. Ilm80Hem20 for $y = 0.8$.

95 At room temperature members of the ilmenite-hematite solid solution series are either
96 para-, ferri-, or antiferromagnetic, depending on their individual cation ordering and spin
97 structure (e.g. McEnroe et al., 2000; Burton et al., 2008). Ilmnohematites with compositions
98 of $0 < y < 0.5$ are antiferromagnetic at room temperature and their magnetic moments are
99 aligned as in hematite (Warner et al., 1972). Ferrimagnetic ordering in hemoilmenite occurs

100 for intermediate compositions ($0.5 < y < 0.8$) and is related to the ordering of Fe and Ti on
101 separate sub-lattices (Ishikawa, 1985; Burton et al., 2008). Compositions with $y > 0.8$ are
102 paramagnetic at room temperature, but magnetic ordering does occur at lower temperatures,
103 e.g. the end-member ilmenite is antiferromagnetic below its Néel temperature of ~ 58 K (Kato
104 et al., 1982).

105 This study has two aims: first to identify the low-temperature remanence and hysteresis
106 characteristics that will help to discriminate between the members of the magnetite-ulvöspinel
107 and ilmenite-hematite solid solution series. This will expand the low-temperature database
108 and therefore our understanding of natural samples. Secondly, the applied low-temperature
109 magnetic measurements provide an insight into the environmental implications for the gravity
110 core retrieved from the Niger deep-sea fan, by demonstrating the compositional changes of
111 the magnetic mineral assemblage during progressive sub- and anoxic diagenesis. The rock
112 magnetic results are linked to findings of quantitative SEM energy dispersive spectroscopy
113 (EDS) analyses. In particular, the intensity ratios of the characteristic Fe K_{α} and Ti K_{α} lines
114 are used to differentiate between the mineral phases of the magnetite-ulvöspinel and ilmenite-
115 hematite solid solution series. This combination of magnetic and electron microscopic
116 techniques is helpful in understanding the post-depositional processes in the sedimentary
117 setting of the Niger deep-sea fan and therefore allows us to draw conclusions on the alteration
118 of the primary continental input.

119

120 **Materials and methods**

121 *Sample selection and treatment*

122 Magnetic extraction following the method of Petersen et al. (1986) was applied to obtain
123 magnetic concentrates for five representative samples along the depth profile of gravity core
124 GeoB 4901 from (a) the upper suboxic sediments above the Fe-redox boundary (1.65 m), (b)

125 the upper suboxic sediments below the Fe-redox boundary (2.95 m), and (c) to (e) from the
126 anoxic sulfidic sediments (13.25, 14.55 and 15.25 m; see Fig. 2). The enrichment of the
127 magnetic fraction was necessary because the starting concentration is too low for meaningful
128 bulk sediment measurements. Mass determination of the extracts is not practical here, since
129 the typical amount for these magnetic extracts is below the precision of a microbalance
130 ($\sigma = 10^{-5}$ g). The sample from 1.65 m depth represents the zone where diagenetic influences
131 are minimal and hence characterizes the primary magnetic mineralogy. The main interest of
132 sampling at 2.95 m was to detect the potential existence of biogenic magnetite, which may
133 form around the modern Fe-redox boundary (Hilgenfeldt, 2000). Samples between 13.25 m
134 and 15.25 m were selected to characterize the magnetic mineral assemblage in the anoxic
135 sediments (Fig. 2).

136

137 *Scanning electron microscopy*

138 SEM analysis included backscatter electron (BSE) imaging (Lloyd, 1985) performed on the
139 magnetic extracts of selected unconsolidated samples from depths of 1.65, 14.55 and 15.25 m
140 depth, using a *FEI XL30 SFEG* scanning electron microscope at the EMU (Electron
141 Microscopy Utrecht, The Netherlands). The SEM was operated at an acceleration voltage
142 between 12 and 30 kV, with a ~2 nA beam current and a spot size of ~0.5 μm . Sample
143 preparation for SEM analysis was carried out as described in Franke et al. (2007a). The
144 elemental composition was acquired using energy X-ray dispersive spectroscopy (EDS;
145 Goldstein et al., 1992). The obtained element spectra were (semi-)quantified using the
146 '*Remote SEM Quant Phiroz*' program version 3.4. All element spectra are normalized to the
147 height of their oxygen peak. Background noise was subtracted before calculation of the
148 element composition. The SEM analyses are restricted to the resolvable μm -particle fraction
149 of the extracts and EDS was performed for about 40 to 50 particles per sample. The upper

150 suboxic environment is represented by the sample from 1.65 m depth. Samples from 14.55 m
151 and 15.25 m depth represent the anoxic zone. In the following the SEM results of the two
152 samples from 14.55 m and 15.25 m depth are combined and will be referred to as anoxic
153 samples.

154

155 *Low-temperature magnetic measurements*

156 Low-temperature magnetic measurements were performed on a superconducting *Quantum*
157 *Design* Magnetic Property Measurement System (MPMS), with an instrumental noise level of
158 $\sim 10^{-11}$ Am². Two types of low-temperature measurements were performed in this study: (1)
159 saturation isothermal remanent magnetization imparted at room temperature (RT-SIRM) by
160 applying a maximum field of 5 T at 300 K followed by continuous cooling in zero field to 5 K
161 and subsequent continuous warming back to 300 K. (2) Hysteresis loops measured between
162 magnetic peak fields of ± 5 T at 15 distinct temperatures between 5 and 295 K. From these
163 loops the temperature dependence of the standard hysteresis parameters such as saturation
164 magnetization (M_S), saturation remanent magnetization (M_{RS}) and coercive force (B_C) were
165 determined.

166

167 **Scanning electron microscopic results**

168 *Discrimination between titanomagnetite and hemoilmenite*

169 Studies such as Franke et al. (2007b) and Lattard et al. (2005) have shown that the EDS
170 intensity ratios of the characteristic Fe K_{α} and Ti K_{α} lines can be used under certain
171 conditions to differentiate between mineral phases of the magnetite-ulvöspinel and ilmenite-
172 hematite solid solution series. Element spectra with high Fe/Ti intensity ratios were found to
173 be rather typical of titanomagnetite while low Fe/Ti ratios are indicative of hemoilmenite.

174 With increasing Ti-content the Fe/Ti ratio decreases for both solid solution series, the lowest
175 possible value is $\text{Fe/Ti} = 2$ for the magnetite-ulvöspinel solid solution series and $\text{Fe/Ti} = 1$ for
176 the ilmenite-hematite solid solution series according to their respective stoichiometric
177 formulas. Ratios of $\text{Fe/Ti} < 1$ constitute members of the ternary system between rutile (TiO_2)
178 and the pseudobrookite-ferropseudobrookite solid solution series (Fe_2TiO_5 - FeTi_2O_5).
179 Therefore particles with ratios of $\text{Fe/Ti} > 2$ could be theoretically either members of the
180 magnetite-ulvöspinel or the ilmenite-hematite solid solution series, while particles with ratios
181 of $1 \leq \text{Fe/Ti} < 2$ can only be members of the ilmenite-hematite solid solution series.

182 To test this method, EDS spectra were taken from a defined synthetic sample (6F72x2.4)
183 of well-known composition, which was provided by the Mineralogical Institute of the
184 University of Heidelberg. The sample was synthesized at 1300°C in the Fe-Ti-O system and
185 contains titanomagnetite (TM63) and synthetic hemoilmenite (= ferrian ilmenite;
186 $\text{Ilm}_{76}\text{Hem}_{24}$). This sample was subsequently used as a pre-defined standard to which the
187 EDS peak intensities of the unconsolidated natural particles of this study were compared.
188 Another advantage of the synthetic sample is its ideal flat polished surface, which means that
189 considerable scattering effects can be neglected.

190 The element spectra were derived on the same SEM instrument for both the synthetic and
191 natural samples. Fig. 3a shows a backscatter electron (BSE) micrograph of the synthetic
192 sample 6F72x2.4. The gray tones in the BSE image reflect the different chemical
193 compositions of the two mineral phases, with lighter areas corresponding to titanomagnetite
194 (Fe-richer areas) and darker areas corresponding to members of the ilmenite-hematite solid
195 solution series (Fe-poorer areas). Completely black or white spots mark pores in the polished
196 sample, where surface charging might have an effect due to poor carbon coating. The two
197 mineral phases can be discriminated by their EDS element spectra (Figs. 3b and 3c), since the
198 intensity ratios of the characteristic Fe K_α and Ti K_α lines are distinct. In Table 1 the semi-

199 quantified Fe and Ti contents are listed for ten spot checks analyzed on the polished section of
200 the synthetic sample. The values were used to calculate the Fe/Ti ratios and the resulting
201 titanomagnetite (TM) and hemoilmenite (IlmHem) mean compositions. Spectra from TM
202 (lighter area) show Fe/Ti ratios > 2 , corresponding to quantitative EDS spectra for which the
203 Fe-peak is equal or higher than the Ti-peak. Spectra from hemoilmenite (darker areas) have
204 ratios $1 \leq \text{Fe/Ti} < 2$, showing Ti-peaks that are much higher than the Fe-peaks. This can be
205 easily explained by the position of the Ti K_{α} (at 5.896 eV) and Fe K_{α} (at 6.403 eV) lines in
206 the spectra, e.g. a particle with the same peak height for both elements contains therefore less
207 Ti than Fe. The average composition of the synthetic sample 6F72x2.4 was calculated as
208 TM68 and Ilm78Hem22. These values are only slightly higher than the compositions (TM63
209 and Ilm76Hem24) derived from published electron microprobe (EMP) analyses and
210 inductively coupled plasma atomic emission spectrometry (ICP-AES) reported by Lattard et
211 al. (2005; 2006). The error of our EDS method is therefore less than 3%. This discrepancy is
212 presumably due to slightly inhomogeneous chemical compositions within the sample from the
213 rim to the center of the synthesized pellet (R. Engelmann, pers. comm., 2006). These results
214 underline that it is in principle possible to discriminate between titanomagnetite and
215 hemoilmenite phases on the basis of the element intensity ratio Fe/Ti, hence that it is possible
216 to calculate a close approximate composition for each individual particle.

217

218 *Magnetic particle discrimination*

219 The selected beam strength between 12 and 30 kV used for the quantitative EDS analysis
220 detects all main elements within the Fe-Ti-O system and furthermore all potential minor
221 element contributions which might be present in the mineral grains. The elements V, Cr, Al
222 and Ti are common substitutions in hematite, whereas Mg and Mn are rather typical

223 constituents in ilmenite. Besides Ti, magnetite may also contain the elements Mg, Mn, Cr and
224 Al.

225 In practice, the analyzed particles from both solid solution series mainly show
226 substitutions of Mg and Al. Other minor element contributions were rarely detected in our
227 samples and were found in less than 20% of all analyzed particles. The contribution of these
228 additional minor elements to the individual EDS spectra is usually less than 3%. Therefore the
229 effect of minor elements other than Al and Mg can be neglected for this study. This concurs
230 with the fact that Mg and Al are the most common cation impurities in natural
231 titanomagnetites and hemoilmenites found in igneous rocks (Creer et al., 1975).

232 Fig. 4a and 4b show the cation element content in at% for the main elements Fe and Ti
233 and the minor abundant elements Mg and Al for all the examined particles, divided into
234 suboxic and anoxic environments. To generally consider the effect of substitution of Fe with
235 either Mg or Al, regardless for which member of both solid solution series, the total of the
236 three elements Fe, Mg and Al was calculated and will be referred to as Fe_{Σ} (= Fe+Al+Mg) in
237 the following interpretations.

238 The magnetic mineral assemblage of the upper suboxic environment is dominated by Fe-
239 rich mineral phases with fairly low Ti-contents (Fig. 4a). In contrast, the Ti-content increases
240 notably and even exceeds the Fe-content in the particles of the lower anoxic samples (Fig.
241 4b). In Fig. 4c and Fig. 4d representative element spectra of typical particles from the
242 magnetic extracts are shown, originating from the upper suboxic and lower anoxic domain.
243 These EDS analyses clearly show that the natural magnetic grains contain minor amounts of
244 other ions than Fe and Ti. The presence of the supplementary elements, such as Na, Mg, Al
245 and Si support the assumption of the detrital origin of these particles. Small amounts of Al
246 and Si are most likely also due to clay mineral coatings on the grains.

247 In Table 1 the element ratios of $\text{Fe}_{\Sigma}/\text{Ti}$ for each analyzed particle are divided into the
248 $\text{Fe}_{\Sigma}/\text{Ti} \geq 2$; $1 \leq \text{Fe}_{\Sigma}/\text{Ti} < 2$; $0.5 \leq \text{Fe}_{\Sigma}/\text{Ti} < 1$ and $\text{Fe}_{\Sigma}/\text{Ti} < 0.5$ fractions. In the upper suboxic
249 zone ~19% of the examined particles exhibit spectra without any Ti-content, comparable to
250 spectrum (1) in Fig. 4c. They represent detrital magnetite, a common component in the upper
251 suboxic core section. However, the majority of the magnetic particles contain Ti, with an
252 element ratio $\text{Fe}_{\Sigma}/\text{Ti}$ varying between 0.75 and 13.89; 79% of these particles have $\text{Fe}_{\Sigma}/\text{Ti}$
253 ratios ≥ 2 , only 2% have $\text{Fe}_{\Sigma}/\text{Ti}$ ratios < 1 (Table 2).

254 According to the (semi-)quantitative EDS spectra, the Ti-content for particles with ratios of
255 $\text{Fe}_{\Sigma}/\text{Ti} \geq 2$ varies between 0.4 and 4.9 at%. As already explained in the precedent section, this
256 could either correspond to a titanomagnetite composition between TM20 and TM90 or
257 to compositions between Ilm13Hem87 and Ilm60Hem40 for members of the ilmenite-hematite
258 solid solution series. For $0 \leq x < 0.75$ these assumed titanomagnetite compositions are
259 conceivable. However, titanomagnetites with $x > 0.75$ are quite uncommon in nature
260 (Petersen and Bleil, 1982). Instead it is more likely that grains with $x > 0.75$ represent
261 hemoilmenite particles instead, which then would correspond to compositions between
262 Ilm50Hem50 and Ilm60Hem40. Hemoilmenites of such compositions are typical for
263 volcanogenic rocks that underwent high-temperature deuteric oxidation processes.

264 We have to keep in mind however, that natural mineral grains of the magnetite-ulvöspinel
265 and ilmenite-hematite solid solution series occur rarely in completely homogenous
266 compositions. In fact paragenesis between Ti-poor (titano-)magnetite or ilmenoematite and
267 Ti-rich hemoilmenite is a common aftereffect of oxy-exsolution of volcanic rocks. Depending
268 on the progression of such alterations, the crystal matrix might contain exsolution lamellae in
269 nano- or even micrometer scale (e.g. McEnroe et al., 2001; Garming et al., 2007). The EDS
270 analyses has a spatial resolution of $\sim 0.5 \mu\text{m}$, therefore it was possible to resolve
271 inhomogeneities up to that limit. Beyond this spatial resolution we might have to deal to a

272 certain degree with overlap analyses, if exsolution features are present in a given grain. For
273 particles larger than 0.5 μm , multiple spot analyses were performed to check local
274 inhomogeneities or to derive average compositions.

275 Additionally, magnetic inclusions in silicates were observed. They make up ~5 % of the
276 magnetic assemblage in the upper suboxic zone. The major elements in the measured spectra
277 are Si and O, which are accompanied by Fe and Ti as minor components. Calculated element
278 compositions for the magnetic inclusions show $\text{Fe}_{\Sigma}/\text{Ti}$ ratios of ≥ 2 , resulting in either TM15
279 to TM60 or alternatively Ilm09Hem91 to Ilm40Hem60. Such typical Ti-poor composites have
280 been found in various sedimentary environments as described by e.g. Garming et al. (2005).

281 Shrinking cracks are evidence for a mild maghemitization (Dunlop and Özdemir, 1997),
282 but only a small number was observed in the upper suboxic sample. This suggests that (titano-
283)maghemite is of low importance in these samples. In addition to the observed microparticles,
284 a considerable number of much smaller grains in the nm-range are present in the sample from
285 the upper suboxic zone. These grains are beyond the spatial resolution of the used SEM. This
286 is indicative for the presence of small PSD/SD particles.

287 In contrast to the analysis of the suboxic sample, only minor amounts of nm-sized particles
288 were observed in the magnetic extracts from 14.55 and 15.25 m. These samples mainly
289 consist of somewhat “coarser” grains in the grain-size range from ~2 to 5 μm . Non-magnetic
290 particles, such as silicates and feldspars are more abundant here than in the upper suboxic
291 sample. This has to be kept in mind for the interpretation of the hysteresis data.

292 The average Ti-content of all particles examined is notably higher for the anoxic samples
293 (~ 4.06 at%) compared to the suboxic samples (~1.61 at%) and even exceeds the meager Fe
294 content (Fig. 4b). When taking the Mg and Al concentrations into account, the mean value of
295 Fe_{Σ} is slightly higher than the average Ti-content.

296 In terms of numbers of grains the Ti-rich mineral phases clearly dominate the (magnetic)
297 mineral inventory in the lower anoxic sediments. Here the ratios Fe_{Σ}/Ti vary between 0.21
298 and 4.87, particles without any Ti-content were no longer observed. Only 24% of the
299 examined grains exhibit Fe_{Σ}/Ti ratios ≥ 2 . These particles would either refer to compositions
300 between TM51 and TM99 or to compositions of Ilm34Hem66 to Ilm66Hem34. Particles with
301 $1 \leq Fe_{\Sigma}/Ti < 2$ (47%) appear to be the most abundant members of the ilmenite-hematite solid
302 solution series. Their Ti-content varies between 0.95 and 7.04 at%, corresponding to
303 Ilm68Hem32 and Ilm99Hem01, respectively.

304 Additionally, a considerable number of particles yield Fe_{Σ}/Ti ratios of < 1 (26%) or even
305 < 0.5 (3%). The element spectra for this particle type exhibit much higher Ti- than Fe-content
306 (Fig. 3; compare spectrum (5)). This composition corresponds rather to the pseudobrookite-
307 ferropseudobrookite solid solution series. Pseudobrookite may be present in the detrital Fe-Ti
308 oxide assemblage as minor constituents within titanomagnetite and -hematite grains as a
309 result of high-temperature oxidation during the initial cooling of igneous rocks (Reynolds and
310 Goldhaber, 1978; Frost and Lindsley, 1991). Another possibility for the genesis of such Ti-
311 rich mineral phases is the further alteration of members of the ilmenite-hematite solid solution
312 series towards hematite with fine rims of anatase (Houston and Murphy, 1962). This would
313 enrich the elemental bulk composition of the grains in terms of their TiO_2 content.

314 The number of silicates with magnetic inclusions was found to be reasonably higher (14%)
315 in the anoxic sediments compared to the suboxic sample (5%). The majority of these
316 inclusions (92%) have Fe_{Σ}/Ti ratios ≥ 2 (resulting in compositions of TM09 to TM75 or
317 Ilm06Hem94 to Ilm50Hem50), only 8% of the inclusions show Fe_{Σ}/Ti ratios of < 1 .

318

319

320 *Summary of SEM results*

321 As mentioned above, titanomagnetites with $x > 0.75$ are quite rare in nature (Petersen and
322 Bleil, 1982). The range of the composition for hemoilmenite strongly relates to the bulk
323 chemistry of the rock, but lies typically above $y = 0.5$ (Petersen and Bleil, 1973). Considering
324 these restrictions, the approximate abundances of the various Fe-Ti oxides in the magnetic
325 mineral assemblage of the investigated samples can be estimated (Table 3).

326 The mineral assemblage of the upper suboxic environment constitutes ~19% magnetite,
327 ~62% titanomagnetite (TM20 to TM70), ~17% hemoilmenite (Ilm50Hem50 to Ilm60Hem40)
328 and ~2% other particles. The composition of magnetic inclusions in the siliceous matrix
329 varies between TM15 and TM60. The main magnetic mineral component in the magnetic
330 assemblage of the lower suboxic environment is hemoilmenite with an abundance of ~66%
331 and compositions varying between Ilm53Hem47 and Ilm99Hem01. Pure magnetite is no
332 longer present and only ~5% titanomagnetite was found. The remaining ~28% are Ti-rich
333 particles, such as (ferro-)pseudobrookite or rutile. When titanomagnetite is preserved as
334 inclusions in a siliceous matrix it apparently withstands diagenetic alteration even in the
335 anoxic environment.

336

337 **Low-temperature magnetic results**

338 *Room-temperature SIRM (RT-SIRM)*

339 Fig. 5 shows the RT-SIRM curves normalized to their initial value at 300 K and the respective
340 derivatives for all analyzed samples. The samples from the suboxic zone (Fig. 5a-b) clearly
341 show ferrimagnetic dominated curves typical of (titano-)magnetite as described by Özdemir
342 and Dunlop (2003) and Kostrov (2003). The RT-SIRM first increases upon cooling, reaching
343 a maximum around 220 K (Fig. 5a) and 230 K (Fig. 5b). According to Dankers (1978) such
344 an increase upon cooling is related to an increase in the spontaneous magnetization of

345 titanomagnetite phases whose Curie point is above the temperature where the remanence is
346 acquired. For such cases the spontaneous magnetization has not reached its maximum
347 intensity at 300 K, which results in an increase while cooling. Upon further cooling the RT-
348 SIRM curves decrease with decreasing temperature. At 5 K some 83% (Fig. 5a) and 69%
349 (Fig. 5b) of the initial RT-SIRM are demagnetized. At 100 to 110 K the maximum gradient of
350 the cooling curve is reached, corresponding to the temperature interval that is indicative for
351 the Verwey structural phase transition of magnetite. This complies with results from zero field
352 cooling (ZFC) and field cooling (FC) thermal demagnetization experiments, published by
353 Dillon and Bleil (2006), which revealed partially suppressed Verwey transitions in the same
354 temperature interval. During warming from 5 to 300 K the RT-SIRM retraces the cooling
355 curve between 5 and 50 K. Upon further warming only limited remanence recovery is
356 observed when passing back through the Verwey transition. At 300 K about 87% (Fig. 5a)
357 and 80% (Fig. 5b) of the initial RT-SIRM is recovered.

358 The RT-SIRM behavior of samples from the anoxic zone differs strongly to that of the
359 samples from the suboxic layers. However, within the anoxic zone all samples (Fig. 4 c-d)
360 reveal very similar low-temperature behavior with comparable remanence memory. The RT-
361 SIRM cooling curves show a continuous gradual increase between 300 and 5 K, where the
362 RT-SIRM is 46 to 69% higher than the initial remanence. Upon warming the curves resemble
363 the corresponding cooling curves back to ~ 100 K. However, above 100 K the warming
364 curves are below the cooling curves. The remanence loss when returning to 300 K accounts
365 for 86 to 89% of the initial RT-SIRM. No specific magnetic transitions were observed on
366 warming, though the first derivatives of samples 13.25 and 15.25 m display an inflection
367 around 210 K. This may be indicative of the transition of hemoilmenite with an approximate
368 composition of $y = 0.85$ from ferrimagnetism / superparamagnetism back to paramagnetism
369 (Burton et al., 2008).

370

371 *Low-temperature magnetic hysteresis*

372 For all five magnetic extracts the temperature dependence of their hysteresis loops was
373 examined between 5 and 295 K. The measured hysteresis loops contain diamagnetic
374 contributions originating from the sample holder (gelatine capsule) and non-ferromagnetic
375 sediment constituents in the extracts such as feldspars and silicates, which to a certain extent
376 were included in the extract. The temperature dependence of the paramagnetic contribution
377 was calculated, using the relationship $m(B,T) = a \cdot \tanh(B/b)$, where $-m(B,T)$ equals the
378 measured magnetic moment in the applied field B at the temperature T , and a and b are
379 constants (Dunlop and Özdemir, 1997). This approach was necessary since the induced
380 magnetization of paramagnetic constituents begins to saturate in high fields at low-
381 temperatures and cannot be approximated with a linear function. Using this approach,
382 excellent fits to the magnetization curves were achieved (Fig. 6).

383 The results of hysteresis measurements for the suboxic and anoxic samples are largely
384 different. To represent the suboxic and anoxic environments, the temperature evolution of the
385 hysteresis loops is shown for the samples from 1.65 m (Fig. 7a) and 15.25 m (Fig. 7b) depth.
386 For the sake of clarity only six selected temperature steps (295 K, 195 K, 110 K, 50 K, 20 K
387 and 5 K) are given here. The hysteresis loops systematically change in shape with decreasing
388 temperature and increasing sediment depth. At room temperature hysteresis loops for all
389 extracts are quite narrow and yield low coercivities. Saturation magnetization is usually
390 reached in low to moderate fields (< 500 mT), which is indicative of the presence of a soft
391 ferrimagnetic mineral phase. With decreasing temperature the loops become more pronounced
392 and wider, in particular, the samples from the anoxic zone exhibit distinct hysteresis at lower
393 temperatures. This effect is most pronounced in the temperature dependence of B_C (Table 4).

394 The temperature dependence of the hysteresis properties quantified after dia- and
395 paramagnetic correction is shown in Fig. 8. Due to the inability of mass determination, the
396 parameters have been normalized to their respective value at 5 K so that the samples can be
397 compared with each other. The absolute values are summarized in Table 4.

398 The saturation magnetization M_S (Fig. 8a) for the suboxic samples shows only subtle
399 temperature variations between 295 and 30 K. Upon further cooling to 5 K an increase of
400 about 20% is observed. In contrast a quasi-continuous increase for M_S with decreasing
401 temperature can be seen for the anoxic samples. At 5 K the values for M_S are about a factor of
402 two to three higher for the anoxic and only 1.15 for the suboxic samples compared to room
403 temperature. However, the complexity of the paramagnetic correction may effect the accurate
404 determination of M_S and thus the results should be treated with caution.

405 Saturation remanence M_{RS} (Fig. 8b) for the suboxic samples increases slightly between
406 295 and 50 K and in a steeper manner below 50 K. M_{RS} seems to reach saturation at very low
407 temperatures, however, the overall increase of two to three times is relatively small. For the
408 anoxic samples a continuous increase with decreasing temperature is observed, with an
409 overall seven-fold increase between 295 and 5 K.

410 At room temperature, values of B_C (Fig. 8c) range between 6 and 13 mT for all samples.
411 Thompson and Oldfield (1986) report this as a typical value for multi-domain magnetite.
412 Upon cooling, B_C varies little between 295 and 50 K. Below 50 K the coercive field starts to
413 increase sharply, reaching values of 50 – 67 mT at 5 K for the suboxic samples and up to
414 140 – 233 mT for the anoxic samples. This equals a four- and seven-fold increase for the
415 suboxic samples and on average 25-fold higher coercivities for all of the anoxic samples. No
416 ordering temperature could be determined from the temperature dependence of the coercivity
417 (such as the magnetic ordering transition from ferrimagnetism to paramagnetism at 210 K for
418 TH80, as seen before in the RT-SIRM cycling experiments, compare to Fig. 5). The distinct

419 increase of B_C below 50 K might potentially be due to the hemoilmenite entering its spin glass
420 state (Burton et al., 2008).

421 The hysteresis loops at certain low-temperatures exhibit a peculiar wasp-waisted shape,
422 which is more pronounced for the anoxic than for the suboxic samples (Fig. 9). Roberts et al.
423 (1995) and Tauxe (1996) describe this phenomenon as indicative for a mixture of relatively
424 high- and low-coercive material. Such a mixture could consist of either distinct magnetic
425 minerals or a bi-modal grain-size distribution of a single magnetic component.

426 Large quantities of superparamagnetic magnetite or hard coercivity particles (such as
427 hematite or goethite) are commonly assumed to be the main reason for wasp-waisted
428 hysteresis loops. In this study these options appear implausible for several reasons: the
429 applied extraction method tends to favor the collection of rather low-coercivity components
430 (Franke et al. 2007b). Moreover, hematite and/or goethite must be a hundred times more
431 abundant in the sediment to rival the magnetization of (titano-)magnetite. Secondly, the
432 observed hysteresis loops become more constricted with decreasing temperature.
433 Superparamagnetic (magnetite) particles are expected to cause constriction in the room
434 temperature loops rather than low-temperature loops because they block at lower temperatures
435 and become stable single domain grains (Dunlop, 1973).

436 An alternative explanation for the wasp-waisted hysteresis loops at low-temperature are the
437 observed Ti-rich hemoilmenites with compositions $0.85 < y < 1$. These members of the
438 ilmenite-hematite solid solution series are paramagnetic at room-temperature but exhibit
439 superparamagnetic properties just below room temperature and their Néel temperature
440 (Ishikawa, 1962) and antiferromagnetic behavior at lower temperatures (Burton et al., 2008).

441

442 **Discussion**

443 SEM analyses have shown, that the predominant magnetic minerals in the upper suboxic
444 sediments are (titano-)magnetites of variable Ti composition. Both, ilmenohematites and
445 hemoilmenites are also present, but relative to (titano-)magnetite they are less abundant and
446 thus less important in this depth interval. Dillon and Bleil (2006) already suggested that the
447 vast majority of the magnetic assemblage reaching the gravity core location was composed of
448 eroded volcanic material originating from the Cameroon Volcanic Line. Herrero-Bervera et
449 al. (2004) and Ubangoh et al. (2005) reported titanomagnetites, both poor and rich in Ti, as
450 the principal magnetic minerals in rocks from the Cameroon volcanics in the drainage area of
451 the Niger River tributaries. Ubangoh et al. (2005) also observed rocks with abundant ilmenite
452 lamellae in the titanomagnetites. Both investigations used Curie temperature experiments
453 above room-temperature for the discrimination of the magnetic particles. Hemoilmenites with
454 high Ti-contents could not be determined by these former studies, as they may actually have
455 Curie temperatures below room-temperature. Combined with our microscopy findings, which
456 show that hemoilmenite is a minor component of the primary magnetic mineral
457 assemblage compared to (titano-)magnetite, sub-room temperature Curie points provide a
458 possible explanation why members of the ilmenite-hematite solid solution series have not
459 been identified previously.

460 In the lower anoxic sediments early diagenetic alteration after deposition has resulted in a
461 more complete depletion of the (titano-)magnetite phase, producing a relative enrichment of
462 the hemoilmenite phase in the strongly diagenetically altered section so that the relative
463 abundance of the hemoilmenite particles increases to ~66%. This change in abundance can be
464 interpreted in terms of selective diagenetic effects on the magnetic mineral assemblage. Dillon
465 and Bleil (2006) reported that reductive diagenesis has extensively affected the magnetic
466 mineral inventory of these organic-rich late Quaternary sediments in the Niger deep-sea fan.

467 Fig. 2b shows the extent of the suboxic zone and the transition to anoxic conditions in the
468 pore water profile of the sedimentary sequence. The rock magnetic investigation showed that
469 diagenetic processes did not act uniformly across the detrital magnetic mineral assemblage,
470 but instead depended strongly on particle size and Ti-content, with the smallest particles
471 dissolving first and the Ti-rich component being the most resistant to the reducing conditions.
472 Another important determining factor is the availability of sulfur in this geochemical system.

473 Due to the already considerable strong alteration of the upper suboxic sediments, one of
474 the main challenges in this study is the generally low magnetic mineral content. Therefore the
475 concentration of magnetic carriers is even lower in the anoxic sediments and only relicts of
476 the primary magnetic mineral assemblage remain. Highly sensitive low-temperature magnetic
477 measurements on the magnetic extracts were therefore required for magnetic mineral
478 identification. These measurements revealed large contrasts between the samples from the
479 suboxic and anoxic layers. This emphasizes that the Fe-Ti oxide phases occur in different
480 proportions in the two different geochemical zonations, which is also reflected in the
481 magnetic behavior of these samples.

482

483 *Suboxic samples*

484 In the upper suboxic sediments (titano-)magnetite particles dominate the low-temperature
485 magnetic characteristics. The increase in the RT-SIRM cooling curves just below room
486 temperature and the broad decrease around 120 K were described by Özdemir and Dunlop
487 (2003) and Kosterov (2003) as characteristic behavior for a mineral assemblages dominated by
488 (Ti-poor) titanomagnetite (Fig. 3). Additionally, the low-temperature hysteresis
489 measurements confirm the presence of a soft ferrimagnetic mineral phase, documented in the
490 relatively small increase in hysteresis parameters with decreasing temperature. The value of
491 the coercive force, showing an overall increase by a factor of four to seven between 300 and

492 5 K, is comparable with results obtained from synthetic magnetites by Özdemir et al. (2002).
493 Harrison and Putnis (1995) analyzed the low-temperature dependence of the magnetite-
494 ulvöspinel solid solution series and observed low coercivities (10 mT) for the magnetite-rich
495 (Fe-rich) endmembers at low-temperatures (4.4 K). The synthetic submicron magnetites in the
496 study of Özdemir et al. (2002) yield coercivities of ~15 mT at room temperature and ~50 mT
497 at 15 K, which is a similar increase in B_C by a factor of three to four. The coercivity of the
498 synthetic samples increases sharply when crossing the Verwey transition because their
499 compositions are close to stoichiometry. The lack of the Verwey transition in the suboxic
500 samples of this study is presumably due to their Ti-content, since at fairly low Ti-contents of
501 $x > 0.04$ the transition is suppressed (Kakol et al., 1994). The small amount of observed
502 shrinking cracks is indicative of a small degree of maghemitization, which may additionally
503 subdue the Verwey transition (Dunlop and Özdemir, 1997). Tucker (1981) reported low-
504 temperature magnetic hysteresis properties for two multi domain titanomagnetite crystals with
505 compositions of $x = 0.52$ and $x = 0.65$. The first titanomagnetite ($x = 0.52$) shows values of
506 B_C (~25 mT) and M_{RS}/M_S (0.29) at 77 K that are comparable with our results at 75 K of
507 $B_C=25$ mT and a M_{RS}/M_S ratio of 0.25. The calculated average titanomagnetite composition
508 for our suboxic mineral assemblage results in a mean value of TM55 which is very close to
509 the composition of the respective single crystal of Tucker (1981). For the TM65 crystal from
510 the study of Tucker (1981) the reported values are higher ($B_C = 58$ mT; $M_{RS}/M_S = 0.58$), with
511 the increased coercivity explained as a result of increasing in magnetic anisotropy. At even
512 lower temperatures of 4.2 K, Schmidbauer and Readman (1982) observed coercivity values of
513 comparable magnitude for titanomagnetites with compositions of $x = 0.5$ ($B_C \sim 31$ mT) and
514 $x = 0.6$ ($B_C \sim 70$ mT).

515 The hysteresis loops of the suboxic samples show wasp-waisted shapes at lower
516 temperatures. The presence of an intermediate titanomagnetite phase in paragenesis with a
517 hemoilmenite phase as described by Krása et al. (2005) would offer a reasonable explanation

518 for this behavior. According to Buddington and Lindsley (1964) the ilmenite content of a
519 hemoilmenite phase coexisting with a titanomagnetite phase with a composition of $x > 0.5$
520 would be $y > 0.85$. Since hemoilmenite phases of $y > 0.87$ exhibit superparamagnetic
521 properties at low-temperatures (Ishikawa, 1962), this could explain the constriction that was
522 observed in the hysteresis loops of the suboxic samples. This is also consistent with the SEM
523 and EDS analyses, which revealed the presence of hemoilmenite as minor constituents
524 (~17%) in the primary magnetic mineral assemblage of the suboxic samples.

525 Nevertheless, the Ti-contents derived from the SEM analysis are not overly high.
526 However, the hysteresis loop for the synthetic sample 6F72x2.4 clearly shows wasp-waisted
527 characteristics at temperatures ≤ 55 K (Fig. 10), even though the composition of the
528 hemoilmenite phase is below $y = 0.8$. With $y = 0.76$ the hemoilmenite composition of
529 6F72x2.4 is still higher than in our natural sample, but it generally shows that wasp-waisted
530 shapes do occur for such Ti-contents. The distribution of the two phases in the synthetic
531 sample is comparable (79% TM : 21% IlmHem) to the derived distribution in our natural
532 suboxic sample (82% Mt/TM : 17% IlmHem). Therefore the wasp-waisted shape in our
533 hysteresis loops is most likely the result from the interplay between titanomagnetite and
534 hemoilmenite.

535

536 *Anoxic samples*

537 The results of the low-temperature measurements from the anoxic layers lead to the
538 conclusion, that titanomagnetite can not be the predominant magnetic mineral phase in this
539 depth interval. Here, Ti-rich hemoilmenite dominates the magnetic mineral assemblage. This
540 was also confirmed by the findings of Heslop and Dillon (2007), who used a non-negative
541 matrix factorization (NMF) algorithm to unmix remanence data into constituent end-members
542 from the same Niger deep-sea fan sediments. Based on the coercivity distribution, fine and

543 coarse grained (titano-)magnetite was found to make the greatest contribution to the
544 remanence signal in the upper sediments. However, a third component was needed to
545 successfully model the detrital magnetic mineral assemblage. This third component
546 comprised the hardest coercivity and was argued to be Ti-rich titanomagnetite or
547 hemoilmenite. It could be shown by the present study, that below the anoxic/sulphidic
548 transition, this Ti-rich component had the highest resistance to reductive dissolution and
549 dominates the magnetic mineral assemblage. The coarse and fine (titano-)magnetite fraction
550 almost disappears completely towards the base of the sediment core.

551 During cooling, the RT-SIRM increases continuously with decreasing temperature. Franke
552 et al. (2007c) considered two possibilities for this phenomenon, either the presence of a high-
553 coercive mineral such as goethite or a Ti-rich oxide phase. Due to their assumption that high-
554 coercivity minerals are generally under-represented in magnetic extracts, it appears more
555 probable for the natural samples in this study that a Ti-rich mineral phase is responsible for
556 the observed increase of RT-SIRM during cooling. The assumption that this behavior can be
557 attributed to the presence of hemoilmenite in our Niger deep-sea fan samples is therefore
558 reasonable, although the interpretation of low-temperature RT-SIRM curves from comparable
559 natural samples is still lacking in the literature (Kosterov, 2007).

560 Fig. 11 compares the low-temperature measurements performed on the natural sample
561 from gravity core GeoB 4901 (15.25 m; Fig. 11a) and the well-defined synthetic sample
562 6F72x2.4 (Fig. 11b). The continuous increasing trend in the RT-SIRM curves with decreasing
563 temperature can be seen for both samples. Since the composition of the synthetic sample is
564 well known, goethite can be excluded as a possible reason for this low-temperature behavior.
565 Here this phenomenon can be rather attributed to the presence of a Ti-rich mineral phase. The
566 RT-SIRM curve of another well-defined single phase titanomagnetite of synthetic origin
567 (TM60) (not shown here; R. Engelmann, unpublished data) shows a rather similar RT-SIRM

568 curve progression as the suboxic samples of this study, with a large decrease around 190 K.
569 This particular sample does not contain any hemoilmenite, therefore we suggest that in the
570 two-phase synthetic sample 6F72x2.4 the distinct low-temperature increase refers to the
571 presence of a Ti-rich hemoilmenite phase.

572 This sample possibly shows paramagnetic-like LT-behavior caused by the presumable
573 presence of near endmember ilmenite. The magnetically harder nature of this mineral phase
574 suggests that a higher coercivity magnetic component other than (titano-)magnetite must be
575 present to create such a low-temperature increase in the RT-SIRM. In particular the EDS
576 results of the SEM analyses confirm an overall higher content of Ti-rich particles in the lower
577 anoxic part of the sediment series. The main component here is hemoilmenite (~66%) with
578 compositions between Ilm50Hem50 up to nearly pure ilmenite (Ilm99Hem01).

579 The unusually high coercivities of the anoxic samples at low-temperatures also concur with
580 the presence of hemoilmenite, rather than titanomagnetite. The stability at low-temperatures
581 with B_C values up to 220 mT is remarkable. For titanomagnetites such high coercivities at
582 low-temperatures have been rarely published in the literature. Schmidbauer and Readman
583 (1982) reported coercive forces of 500 mT for synthetic titanomagnetites with a composition
584 of $x = 0.8$ at 4.2 K, which is twice as high as the natural samples in our study.

585 Brown et al. (1993) also reported coercivity values for members of the ilmenite-hematite
586 solid solution series. For synthetic ilmenoهماتites (= titanohematites) with compositions of
587 $y = 0.2$ and $y = 0.4$ to 0.6 they observed values between 170 mT and 260 mT at temperatures
588 of 125 K. They also found that samples quenched at high-temperatures have significantly
589 higher coercivities than those annealed at temperatures below the order-disorder transition of
590 hemoilmenite. Nord and Lawson (1992) correlate this behavior to the development of twin
591 domain boundaries during quenching from high-temperature, and suggest that annealing

592 above the order-disorder transition temperature results in a substantial increase in twin-
593 domain boundaries and a drastic increase in the coercivity of the material.

594 Gehring et al. (2007) studied micromagnetic properties of ilmenite-hematite particles
595 originating from an alluvial soil. X-ray diffraction revealed hemoilmenite grains with an
596 ilmenite mole fraction of $y = 0.86$. The hysteresis loops at 20 K yielded $B_C = 92\text{mT}$, reached
597 $B_C = 144\text{ mT}$ at 15 K, and $B_C = 244\text{ mT}$ at 6 K. These values are clearly consistent with the
598 results of our study (compare Table 2). Here, the calculated average hemoilmenite
599 composition is $\text{Ilm}_{77}\text{Hem}_{23}$. In metamorphic ilmenite-hematite bearing rocks from Norway
600 stable natural remanences have been identified by McEnroe et al. (2001). Such natural phases
601 show high coercivities that are attributed to their small grain-sizes (Merrill, 1968, McEnroe et
602 al., 2001).

603 Besides the unusually high coercivities of the natural samples, the wasp-waisted shape of
604 the low-temperature hysteresis loops hints at the presence of Ti-rich hemoilmenite phases. For
605 the suboxic samples the wasp-waisted shape could be explained by the interaction between
606 titanomagnetite and hemoilmenite. In the anoxic sediments titanomagnetite is only present in
607 very minor amounts (~5%), but wasp-waisted hysteresis loops are still observed. These are
608 most pronounced in the temperature interval between 30 and 50 K. Apparently, another
609 mechanism must be responsible for this phenomenon. The hysteresis loops measured by
610 Gehring et al. (2007) showed typical wasp-waisted shapes at temperatures between 150 and
611 30 K, which became more pronounced with decreasing temperature. They explained the
612 wasp-waisted shape by the generation of short-range ordered areas in the superparamagnetic
613 state within the hemoilmenite particles.

614 Hemoilmenites with $0.8 \leq y \leq 0.87$ are known to exhibit superparamagnetic behavior at
615 temperatures below 50 K (Ishikawa et al., 1985) and thus can account for the wasp-waisted
616 shape of the hysteresis loops at low-temperatures. Such Ti-rich phases are rather untypical as

617 individual homogenous grains, but are more likely to be present as intergrown exsolution
618 lamellae within the Ti-poor ilmenohematite matrix. Dunlop and Özdemir (1997) report that if
619 the cooling of a melt is slow enough, hemoilmenite of intermediate composition tends to
620 exsolve into intergrown Ti-poor (near hematite) and Ti-rich (near ilmenite) phases. However,
621 compositions with $y > 0.8$ were identified in the magnetic extracts of this study. Whether they
622 consist of either homogenous grains or of intergrown exsolved phases cannot be verified by
623 the technique used for our unconsolidated samples but it seems very likely.

624 Nord and Lawson (1992) reported that hemoilmenites with $y > 0.5$ are magnetically
625 inhomogeneous and consist of cation-ordered ferrimagnetic microstructures which are
626 separated by boundary layers. Earlier, Lawson and Nord (1984) showed that synthetic
627 Ilm80Hem20 ($y = 0.8$) samples had remanence properties that can be explained by the
628 presence of a single SD-like magnetic carrier, even though Ilm80Hem20 should be
629 paramagnetic at room temperature. The source of the measured remanence is argued to be
630 SD-like material within the grains themselves, resulting from the generation of transformation
631 induced domain boundaries, which are partly enriched in the hematite component relative to
632 the bulk composition of the grain.

633 Specific low-temperature magnetic measurements can be used to differentiate between Fe
634 and Ti dominated magnetic mineral assemblages. If Fe-rich mineral phases prevail, RT-SIRM
635 cycles in the low-temperature range show a distinct decrease around the Néel temperature
636 and/or Verwey transition of magnetite. For Ti-rich particles the RT-SIRM curves
637 continuously increase with decreasing temperature. However, solely on the basis of the RT-
638 SIRM experiments it is not possible to differentiate unambiguously between the magnetite-
639 ulvöspinel ($\text{Fe}_{3-x}\text{Ti}_x\text{O}_4$) and ilmenite-hematite solid solution series ($\text{Fe}_{2-y}\text{Ti}_y\text{O}_3$). The hysteresis
640 parameters reveal additional diagnostic features that can help to differentiate between Fe-rich
641 and Ti-rich oxide mineral phases. The characteristic evolution of the measured loops with

642 decreasing temperature points towards two distinct mineral phases in the different
643 environments. In particular the coercive force was found to be a helpful indicative parameter,
644 with a 25-fold increase characteristic of phases from the ilmenite-hematite solid solution
645 series. Such high values were not found for any Fe-rich mineral phase. The high coercivities
646 most likely result from exsolution or lamellar magnetism in hemoilmenite grains.

647

648 *Environmental implication: correlation of Fe and Ti vs. κ*

649 EDS analyses have clearly shown, that Fe-rich particles dominate the magnetic mineral
650 assemblage in the upper suboxic environment, whereas Ti-rich particles prevail in the lower
651 anoxic section. The dominance of Ti-rich magnetic particles in the lower anoxic environments
652 is also strongly reflected in the downcore profile of the volume magnetic susceptibility κ .
653 Fig. 12 (left) shows the downcore profiles of κ compared to the solid phase concentrations of
654 Fe and Ti in the bulk sediments derived from ICP-EAS analysis (Zabel et al., 2001).

655 The correlation between κ and Fe is in general clear throughout the whole depth profile, as
656 is the correlation between κ and Ti. Only for the depth interval from the top of the core to the
657 modern Fe-redox boundary (upper three meters) is the correlation not significant. However,
658 for this section the correlation is higher between κ and Fe ($r = 0.17$, Pearson; Fig. 12d)
659 relative to the correlation between κ and Ti ($r = 0.05$; Fig. 12e). Below the modern Fe-redox
660 boundary the correlation between κ and Ti is consistently higher than between κ and Fe. Not
661 including the upper three meters, Pearson's correlation coefficient between κ and Ti ($r = 0.70$)
662 is noticeably higher than between κ and Fe ($r = 0.51$).

663 Between 3.0 and 12.5 m core depth the correlation of κ and Ti is considerably higher
664 ($r = 0.79$) than for κ and Fe ($r = 0.29$; Fig. 12d-e). This suggests that below the modern Fe-
665 redox boundary the relative contribution of Ti-rich mineral phases to the magnetic

666 susceptibility signal increases notably. The transition from suboxic to anoxic sedimentary
667 conditions is located at 12.5 m core depth. Below this transition the highest correlation of
668 $r = 0.86$ exists between κ and Ti. For the same depth interval the correlation also increases
669 slightly again for κ and Fe ($r = 0.59$; Fig. 12d). Here, iron is mainly bound to non-magnetic
670 phases such as pyrite, which was identified in previous high-temperature thermomagnetic
671 measurements (Dillon and Bleil, 2006). This agrees well with the fact that the magnetic
672 susceptibility of hemoilmenites ($\chi = 100 - 100000 \cdot 10^{-8} \text{ m}^3/\text{kg}$; Bleil und Petersen, 1982) is at
673 least one magnitude higher compared to the magnetic susceptibility of pyrite ($\chi = 30 \cdot 10^{-8}$
674 m^3/kg ; Thompson and Oldfield, 1982).

675 In the uppermost core section above the modern Fe-redox boundary, the good correlation
676 between κ and Fe implies that reactive Fe is bound in Fe-rich magnetic mineral phases. These
677 phases dominate the magnetic mineral assemblage, both in concentration and concerning their
678 magnetic properties.

679 In the subsequent lower suboxic and anoxic intervals the clear correlation between κ and
680 Ti and the less pronounced correlation between κ and Fe demonstrates that most of the Fe is
681 bound to phases that are non-magnetic at room-temperature or is present in its reduced state.
682 Here reactive Fe was subsequently depleted, relocated and the formation of secondary Fe
683 minerals took place. As a consequence the influence of the Ti-rich phases on the magnetic
684 signal increases significantly. This is also reflected in the magnetic susceptibility record.
685 Therefore we conclude that the degree of correlation between κ and Fe, and Fe and Ti,
686 represents whether the magnetic assemblage is dominated rather by Fe-rich magnetic mineral
687 phases, components of intermediate Ti-content, depleted in reactive Fe, or by Ti-rich
688 magnetic phases, including mainly non-reactive Fe.

689 **Conclusions**

690 In this study the different magnetic components in sediments from the Niger deep-sea fan
691 were determined in detail by a combination of low-temperature measurements with scanning
692 electron microscopy analyses applied to magnetic extracts from various geochemical zones.

693 The magnetic analyses indicate a fairly complex mineralogy of the primary magnetic
694 mineral assemblage, which is dominated by (titano-)magnetite of variable composition
695 derived from the Cameroon volcanics in the drainage area of the Niger River tributaries
696 (Herrero-Bervera et al., 2004; Ubangoh et al., 2005). Above the modern redox boundary
697 hemoilmenite originating from the same source area is also present. Magnetically this phase
698 does not play such an important role here because the concentration is too low and the
699 magnetic moment is too weak.

700 Nevertheless, below 3.0 m core depth, processes of reductive diagenesis start to influence
701 the composition of the magnetic mineral assemblage. The portion of Fe-oxides decreases
702 almost to zero and Ti-bearing mineral phases become more important in this depth interval.
703 Although hemoilmenites are abundant, titanomagnetites are still the major contributor to the
704 magnetic signal.

705 Below the sulfidic transition, located in a depth of 12.5 m, grains of the ilmenite-hematite
706 solid solution series are found to be the prevailing contributor to the magnetization of the
707 anoxic sediments. In the course of reductive diagenesis, alteration has resulted here in a more
708 complete depletion of titanomagnetite. (Titano-)magnetite is most likely replaced by
709 paramagnetic iron sulphide minerals. Hemoilmenite is therefore much more resistant to
710 reductive diagenesis due to its low content of reactive iron.

711 The study has also shown that even when remanence transitions and susceptibility peaks
712 are not obviously apparent in low-temperature data - which is the case for many marine
713 sediment samples - careful investigations of the data reveal important relevant information.

714 This can be used to characterize magnetic mineral phases in a sediment sample and results
715 therefore in a detailed paleoenvironmental understanding.

Accepted Manuscript

716 **Acknowledgements**

717 The synthetic sample 6F72x2.4 and the respective unpublished data were provided by Ralf
718 Engelmann and Dominique Lattard (University Heidelberg, Germany), the authors are grateful
719 for their support and various discussions. We would like to thank T. Frederichs (University of
720 Bremen, Germany) for technical assistance and annotation of the low-temperature MPMS
721 analyses. The SEM and EDS analyses were performed at the EMU (Utrecht University, the
722 Netherlands). The authors would like to thank F. Lagroix and an anonymous reviewer for
723 their helpful comments and U. Bleil for constructive criticism of the manuscript. This study
724 was funded by the DFG (RCOM contribution xxxx).

Accepted Manuscript

725 **References**

- 726 Adegbe, A.T., 2001. Reconstruction of paleoenvironmental conditions in equatorial Atlantic
727 and the Gulf of Guinea Basins for the last 245,000 years. *Berichte, Fachbereich*
728 *Geowissenschaften, Universität Bremen*, 178: 113 pp.
- 729 Bleil, U., and Petersen, N., 1982. Magnetic properties of minerals. In: G. Angenheister
730 (Editor). *Numerical Data and Functional Relationships in Science and Technology*,
731 *Landolt-Börnstein V/1b. Springer-Verlag, Berlin, Heidelberg*, 308-365.
- 732 Bozorth, R.M., Walsh, D.E., and Williams, A.J., 1957. Magnetization of ilmenite-hematite
733 system at low temperatures. *Phys. Rev.*, 108: 157-158.
- 734 Brown, N.E., Navratsky A., Nord Jr., G.L., and Banerjee, S.K., 1993. Hematite-ilmenite
735 (Fe₂O₃-FeTiO₃) solid solutions: Determination of the Fe-Ti order from magnetic
736 properties. *Am. Mineral.*, 78: 941-951.
- 737 Buddington, A., and Lindsley, D., 1964. Iron-titanium oxide minerals and synthetic
738 equivalents. *J. Petrol.*, 5: 310–357.
- 739 Burton, B.P., Robinson, P., McEnroe, S.A., Fabian, K., and Ballaran, T.B., 2008. A low-
740 temperature phase diagram for ilmenite-rich compositions in the system Fe₂O₃-FeTiO₃,
741 *Am. Min.*, in press.
- 742 Canfield, D.E., and Berner, R.A., 1987. Dissolution and pyritization of magnetite in anoxic
743 marine sediments. *Geochim. Cosmochim. Acta*, 51: 645-659.
- 744 Creer, K.M., and Like, C.B., 1967. A low temperature investigation of the natural remanent
745 magnetization of several igneous rocks. *Geophys. J. R. Astr. Soc.*, 12: 301-312.
- 746 Dankers, P.H.M., 1978. Magnetic properties of dispersed natural iron-oxides of known grain-
747 size. Ph.D thesis, State University of Utrecht, 142 pp.

- 748 Dillon, M., and Bleil, U., 2006. Rockmagnetic signatures in diagenetically altered sediments
749 from Niger deep-sea fan. *J. Geophys. Res.*, 111, B03105, doi:10.1029/2004JB003540.
- 750 Dunlop, D.J., 1973. Superparamagnetic and single-domain threshold sizes in magnetite. *J.*
751 *Geophys. Res.*, 78: 1780-1793.
- 752 Dunlop, D.J., and Özdemir, Ö., 1997. *Rock Magnetism: Fundamentals and Frontiers.*
753 Cambridge University Press, Cambridge, 573 pp.
- 754 Franke, C., von Dobeneck, T., Drury, M.R., Meeldijk, J.D., and Dekkers, M.J., 2007a.
755 Magnetic Petrology of Equatorial Atlantic Sediments: Electron Microscopic Results and
756 their Environmental Magnetic Implications, *Paleoceanography*, 22, PA4207,
757 doi:10.1029/2007PA001442.
- 758 Franke, C., Pennock, G.M., Drury, M.R., Engelmann, R., Lattard, D., Garming, J.F.L., von
759 Dobeneck, T., and Dekkers, M.J., 2007b. Identification of magnetic Fe-Ti oxides in marine
760 sediments by electron backscatter diffraction in scanning electron microscopy. *Geophys. J.*
761 *Int.*, 170 (2): 545-555. doi:10.1111/j.1365-246X.2007.03410.x.
- 762 Franke, C., Frederichs, T., and Dekkers, M.J., 2007c. Efficiency of heavy liquid separation to
763 concentrate magnetic particles. *Geophys. J. Int.*, 170 (3): 1053-1066. doi: 10.1111/j.1365-
764 246X.2007.03489.x.
- 765 Frost, B.R., and Lindsley, D.H. 1991. Occurrence of iron-titanium oxides in igneous rocks:
766 *Rev. Mineral.*, 25: 433-468.
- 767 Intergovernmental Oceanographic Commission, 1994. *GEBCO Digital Atlas [CD-ROM].*
768 Intergov.Oceanogr. Comm., Int. Hydrogr. Org., Birkenhead, U.K.
- 769 Gehring, A.U., Fischer, H., Schill, E., Granwehr, J., and Luster, J., 2007. The dynamics of
770 magnetic ordering in a natural hemo-ilmenite solid solution. *Geophys. J. Int.*, 169 (3): 917-
771 925. doi: 10.1111/j.1365-246X.2007.03326.x.

- 772 Goldstein, J.I., Newbury, D.E., Echlin, P., Joy, D.C., Romig Jr., A.D., Lyman, C.E., Fiori, C.,
773 and Lifshin, E., 1992. Scanning electron microscopy and X-ray microanalysis, 2nd edition.
774 Plenum Press, New York, 820 pp.
- 775 Garming, J.F.L., Bleil, U., and Riedinger, N., 2005. Alteration of magnetic mineralogy at the
776 sulphate-methane transition: analysis of sediments from the Argentine continental slope.
777 *Phys. Earth Planet. Inter.*, 151: 290-308.
- 778 Garming, J.F.L., von Dobeneck, T., Franke, C., and Bleil, U., 2007. Low-temperature partial
779 magnetic self-reversal in marine sediments by magnetostatic interaction of titanomagnetite
780 and titanohematite intergrowths. *Geophys. J. Int.*, 170 (3): 1067-1075. doi: 10.1111/j.1365-
781 246X.2007.03504.x.
- 782 Harrison, R.J., and Putnis, A., 1995. Magnetic properties of the magnetite-spinel solid
783 solution: Saturation magnetization and cation distribution. *Am. Mineral.*, 80: 213-221.
- 784 Herrero-Bervera, E., Ubangoh, R., Aka, F.T., and Valet, J.-P., 2004. Paleomagnetic and
785 paleosecular variation study of the Mt. Cameroon volcanics (0.0-0.25 Ma), Cameroon,
786 West Africa. *Phys. Earth Planet. Int.*, 147: 171-182.
- 787 Heslop, D., and Dillon, M., 2007. Unmixing magnetic remanence curves without a priori
788 knowledge. *Geophys. J. Int.*, 170 (2): 556–566. doi:10.1111/j.1365-246X.2007.03432.x.
- 789 Heuer, V., 2003. Spurenelemente in Sedimenten des Südatlantik. Primärer Eintrag und
790 frühdiagenetische Überprägung. *Berichte, Fachbereich Geowissenschaften, Universität*
791 *Bremen*, 209: 136 pp.
- 792 Hilgenfeldt, K., 2000. Diagenetic dissolution of biogenic magnetite in surface sediments of
793 the Beguela upwelling system. *Int. J. Earth Sci.*, 88: 630-640.
- 794 Houston, R.S., and Murphy, J.F., 1962. Titaniferous black sandstone deposits of Wyoming.
795 *Geol. Soc. Wyoming Bull.*, 49: 120 pp.

- 796 Ishikawa, Y., 1962. Magnetic properties of ilmenite-hematite system at low temperature. J.
797 Phys. Soc. Jpn., 17, 1835-1844.
- 798 Ishikawa, Y., Saito, N., Arai, M., Watanabe, Y., and Takei, H., 1985. A new spin glass system
799 of $(1-x)\text{FeTiO}_3\text{-Fe}_2\text{O}_3$. I. Magnetic Properties. J. Phys. Soc. Jpn., 54: 312-325.
- 800 Kakol, Z., Sabol, J., Kozlowski, A., and Honig, J.M., 1994. Influence of titanium doping on
801 the magnetocrystalline anisotropy of magnetite. Phys. Rev. B, 49: 12,767-12,772.
- 802 Karlin, R., and Levi, S., 1985. Geochemical and sedimentological control of the magnetic
803 properties of hemipelagic sediments. J. Geophys. Res., 90: 10,373-10,392.
- 804 Kato, H., Yamada, M., Yamauchi, H., Hiroyoshi, H., Takei, H. and Watanabe, H., 1982.
805 Metamagnetic Phase Transitions in FeTiO_3 . J. Phys. Soc. Jpn., 51: 1769-1777.
- 806 Kostrov, A., 2003. Low-temperature magnetization and AC susceptibility of magnetite:
807 effect of thermomagnetic history. Geophys. J. Int., 154: 58-71.
- 808 Kostrov, A., 2007. Low-temperature magnetic properties, in: D. Gubbins and E. Herrero-
809 Bervera (Editors). Encyclopedia of Geomagnetism and Paleomagnetism, Springer,
810 Dordrecht, The Netherlands, 515-525.
- 811 Krása, D., Shcherbakov, V.P., Kunzmann, T., and Petersen, N., 2005. Self-reversal of
812 remanent magnetization in basalts due to partially oxidized titanomagnetites. Geophys. J.
813 Int., 162: 115-136.
- 814 Lattard, D., Sauerzapf, U., and Käsemann, M., 2005. New calibration data for the Fe-Ti oxide
815 thermo-oxybarometers from experiments in the Fe-Ti-O systems at 1 bar, 1,000-1,300°C
816 and a large range of oxygen fugacities. Contrib. Mineral Petrol., 149: 735-754.
- 817 Lattard D., Engelmann, R., Kontny, A., and Sauerzapf, U., 2006. Curie temperatures of
818 synthetic titanomagnetites in the Fe-Ti-O system: Effects of composition, crystal

- 819 chemistry, and thermomagnetic methods. *J. Geophys. Res.*, 111, B12S28.
820 doi:10.1029/2006JB004591.
- 821 Lloyd, G.E., 1985. Review of instrumentation, techniques and applications of SEM in
822 mineralogy. In: J.C. White (Editor). *Application of electron microscopy in Earth Sciences*.
823 *Min. Ass. of Canada short courses*, 11: 151-188.
- 824 Lagroix, F., Banerjee, S.K., and Jackson, M.J., 2004. Magnetic properties of the Old Crow
825 Tephra: Identification of a complex iron titanium oxide mineralogy. *Geophys. Res.*, 109,
826 B01104, doi:1029/2003JB002678.
- 827 Lawson, C.A., and Nord Jr., G.L., 1984. Remanent magnetization of a “paramagnetic”
828 composition in the ilmenite-hematite solid solution series. *Geophys. Res. Lett.*, 11: 197-
829 200.
- 830 McEnroe, S.A., Robinson, P., and Panish, P., 2000. Detailed chemical and petrographic
831 characterization of ilmenite-and magnetic-rich cumulates of the Sokndal region, Rogaland,
832 Norway. *Norwegian Geolog. Survey Bull.*, 426: 49–56.
- 833 McEnroe, S.A., Robinson, P., and Panish, P.T., 2001. Aeromagnetic anomalies, magnetic
834 petrology, and rock magnetism of hemo-ilmenite- and magnetite-rich cumulate rocks from
835 the Sokndal Region, South Rogaland, Norway. *Am. Mineral.*, 86: 1447-1468.
- 836 Merrill, T.M., 1968. A possible source for the coercivity of ilmenite-hematite minerals. *J.*
837 *Geomagn. Geoelectr.*, 20: 181-185.
- 838 Nord., G.L. Jr., and Lawson, C.A., 1989. Order-disorder transition induced twin domains and
839 magnetic properties in ilmenite-hematite. *Amer. Min.*, 74: 160-176.
- 840 Nord, G.L., Jr., and Lawson, C.A., 1992. Magnetic properties of ilmenite⁷⁰-hematite³⁰:
841 Effect of transformation-induced twin boundaries. *J. Geophys. Res.*, 97: 10897-10910.

- 842 Özdemir, Ö., and Dunlop, D.J., 2003. Low-temperature behavior and memory of iron-rich
843 titanomagnetites (Mt. Haruba, Japan and Mt. Pinatubo, Phillipines. *Earth Planet. Science*
844 *Let.*, 216: 193-200.
- 845 Özdemir, Ö., Dunlop, D.J., and Moskowitz, B.M., 2002. Changes in remanence, coercivity
846 and domain state at low temperatures in magnetite. *Earth Planet. Science Let.*, 194: 343-
847 358.
- 848 Petersen, N., and Bleil, U., 1973. Self reversal of remanent magnetization in synthetic
849 titanomagnetites, *Z. Geophys.*, 39: 965-977.
- 850 Petersen, N., and Bleil, U., 1982. Magnetic properties of rocks. In: G. Angenheister (Editor).
851 *Numerical Data and Functional Relationships in Science and Technology*, Landolt-
852 *Börnstein V/1b*. Springer-Verlag, Berlin, Heidelberg, 366-432.
- 853 Petersen, N., von Dobeneck, T., and Vali, H., 1986. Fossil bacterial magnetite in deep-sea
854 sediments from the South Atlantic Ocean, *Nature*, 320: 611-615.
- 855 Reynolds, R.L., and Goldhaber, M.A., 1978. Iron-titanium minerals and associated alteration
856 phases in some uranium bearing sandstones. *J. Res. U.S. Geol. Surv.*, 6: 707-714.
- 857 Roberts, A.P., Cui, Y., and Verosub, K.L., 1995. Wasp-waisted hysteresis loops: Mineral
858 magnetic characteristics and discrimination of components in mixed magnetic systems. *J.*
859 *Geophys. Res.*, 100: 17909-17924.
- 860 Schmidbauer, E., and Readman, P.W., 1982. Low temperature magnetic properties of Ti-rich
861 Fe-Ti spinels. *J. Magn. Magn. Mat.*, 27: 114-118.
- 862 Schulz, H.D., and cruise participants, 1998. Report and preliminary results of Meteor Cruise
863 M 41/1, *Berichte, Fachbereich Geowissenschaften, Universität Bremen*, 114: 124 pp.
- 864 Tauxe, L., Mullender, T.A.T., and Pick, T., 1996. Potbellies, wasp-waists, and super-
865 paramagnetism in magnetic hysteresis. *J. Geophys. Res.*, 101: 571-583.

- 866 Thompson, R., and Oldfield, F., 1986. Environmental Magnetism. Allen and Unwin, London,
867 227 pp.
- 868 Tucker, P., 1981. Low-temperature magnetic hysteresis properties of multidomain single-
869 crystal titanomagnetite. *Earth Planet. Sci. Lett.*, 54: 167-172.
- 870 Ubangoh, R.U., Pacca, I.G., Nyobe, J.B., Hell, J., and Ateba, B., 2005. Petromagnetic
871 characteristics of Cameroon Line volcanic rocks. *J. Volc. Geotherm. Res.*, 142: 225-241.
- 872 Warner, B.N., Shive, P.N., Allen, J.L., and Terry, C., 1972. A study of the hematite-ilmenite
873 series by the Mössbauer effect. *J. Geomag. Geoelec.*, 24: 353-367.
- 874 Zabel, M., Schneider, R.R., Wagner, T., Adegbe, A.T., de Vries, U., and Kolonic, S., 2001.
875 Late Quaternary climate changes in central Africa as inferred from terrigenous input to the
876 Niger Fan. *Quat. Res.*, 56: 207-217.

877 **Figure captions**

878 Fig. 1 Location of sediment coring site GeoB 4901 in 2184 m water depth on the
879 southeastern flank of Niger deep-sea fan (02°40.7'N / 06°43.2'E). Isobaths are shown at
880 1000 m intervals according to GEBCO Digital Atlas (1994).

881 Fig. 2 (a) Depth profile of the volume specific bulk susceptibility κ delineating variations in
882 the concentration of magnetic minerals. (b) Pore water chemistry at Site GeoB 4901 (Heuer,
883 2003). All parameters are plotted against a linear depth scale and a non-linear age scale
884 (Adegbe, 2001) including marine oxygen isotope stages (MIS) and terminations (T). Grey
885 shading indicates cold periods. Horizontal hatched bars mark the modern iron redox boundary
886 (~2.85 m) and the suboxic / sulfidic anoxic transition (~12.5 m). Arrows at the κ profile
887 denote the horizons, where detailed magnetic analyses have been performed.

888 Fig. 3 (a) Backscattered electron micrograph of synthetic sample 6F72x2.4, light grey areas
889 correspond to TM63 (Fe-richer) and darker grey areas correspond to Ilm76Hem24 (Fe-
890 poorer). (b) EDS spectrum of the TM63 phase from the spot marked in (a). (c) EDS spectrum
891 of the Ilm76Hem24 phase from the spot marked in (a).

892 Fig. 4 Univariate box-and-whisker plots of the cation element content for the main elements
893 Fe and Ti and minor contributions of Mg and Al of magnetic extracts from (a) the suboxic
894 and (b) the anoxic sediments. Fe_{Σ} equals the sum of the three elements Fe, Mg and Al. The
895 boxes represent the median values and the interquartile range, the whiskers mark the total data
896 range. Symbols (+) display outlier samples from the respective data group. (c) and (d) show
897 typical element spectra for particles representing the different Fe-Ti oxide phases detected in
898 the two geochemical environments.

899 Fig. 5 Temperature variation of RT-SIRM during zero field cooling from 300 to 5 K (black
900 solid line) and zero field warming back to 300 K (grey solid line). First derivative curves of
901 the RT-SIRM curves are shown as dashed lines with the same color code.

902 Fig. 6 Uncorrected (black solid line), linear slope corrected (grey solid line) and
903 paramagnetic slope corrected (grey dashed line) hysteresis data shown for samples from (a)
904 1.65 m and (b) 15.25 m core depth measured at 5 K. Filled triangles indicate the high field
905 slopes determined by least squares fit of data measured between 4 and 5 T; filled diamonds
906 depict the paramagnetic slopes derived from the equation $m(B,T) = a \cdot \tanh(B/b)$.

907 Fig. 7 Low-temperature evolution of hysteresis loops for magnetic extracts from samples of
908 the upper suboxic (a, b) and lower anoxic (c, d) core sections. For the sake of clarity,
909 hysteresis loops at six selected temperatures are shown, indicated by small numbers in the left
910 side panel. Data shown on the left are uncorrected, data on the right are corrected for dia- and
911 paramagnetic contributions.

912 Fig. 8 Results of normalized hysteresis parameters: low-temperature dependence of (a)
913 saturation magnetization M_S , (b) saturation remanent magnetization M_{RS} , and (c) coercive
914 field B_C .

915 Fig. 9 Uncorrected hysteresis loops measured at 50 K; suboxic samples (a) and (b) show
916 slightly wasp-waisted characteristics, whereas anoxic samples (c) to (e) show a distinct wasp
917 waisted shape.

918 Fig. 10 Low-temperature hysteresis loops for synthetic sample 6F72x2.4 measured at 55 K
919 (black solid line) and 5 K (grey solid line), showing slightly (55 K) and pronounced (5 K)
920 wasp-waisted shapes (R. Engelmann et al., unpublished data).

921 Fig. 11 Low-temperature variation of RT-SIRM for (a) the magnetic extract from 15.25 m
922 depth and (b) the synthetic sample 6F72x2.4 (R. Engelmann et al., unpublished data).

923 Fig. 12 (left) Downcore profiles of (a) volume magnetic susceptibility κ and solid phase
924 concentrations of (b) Fe and (c) Ti (Zabel et al., 2001). All parameters are plotted on a linear
925 depth scale and a non-linear age scale (Adegbie, 2001) including marine oxygen isotope
926 stages (MIS) and terminations (TI, TII). Grey shading indicates cold periods. For further

927 details see also Figure 2. (right) Correlation of (d) κ vs. Fe-content, and (e) κ vs. Ti-content.
928 Symbols indicate data points for the upper three metres (triangles), the depth interval from
929 3.0 m to 12.5 m (open diamonds) and below 12.5 m (filled diamonds). Pearson's correlation
930 coefficients r are given for the respective depth intervals.

Accepted Manuscript

931 Table 1 Cation element content in at% for the elements Fe and Ti of the synthetic sample
 932 6F72x2.4.

Sample Name	Spot	Ti [at%]	Fe [at%]	Fe/Ti	TM calculated	IlmHem calculated
6F72x2.4	lighter area	TM	4.70	17.51	3.73	63
6F72x2.4	darker area	IlmHem	8.53	12.67	1.49	80/20
6F72x2.4	lighter area	TM	4.75	16.51	3.48	67
6F72x2.4	darker area	IlmHem	8.06	12.53	1.55	78/22
6F72x2.4	darker area	IlmHem	7.96	12.62	1.59	77/23
6F72x2.4	lighter area	TM	4.83	16.25	3.36	69
6F72x2.4	lighter area	TM	5.20	17.53	3.37	69
6F72x2.4	lighter area	TM	5.23	18.57	3.55	66
6F72x2.4	darker area	IlmHem	7.96	12.73	1.60	77/23
6F72x2.4	lighter area	TM	4.81	17.28	3.59	65

933

934

935 Table 2 Distribution of the Fe_{Σ}/Ti ratio for N particles examined.

	N	$Fe_{\Sigma}/Ti < 0.5$	$Fe_{\Sigma}/Ti < 1$	$Fe_{\Sigma}/Ti < 2$	$Fe_{\Sigma}/Ti \geq 2$	$Ti/Fe_{\Sigma} = 0$
<i>Suboxic particles</i>	53	-	2 %	-	79 %	19 %
<i>Silicates</i>	3	-	-	-	100 %	-
<i>Anoxic particles</i>	74	3 %	26 %	47 %	24 %	-
<i>Silicates</i>	12	-	8 %	-	92 %	-

936

937

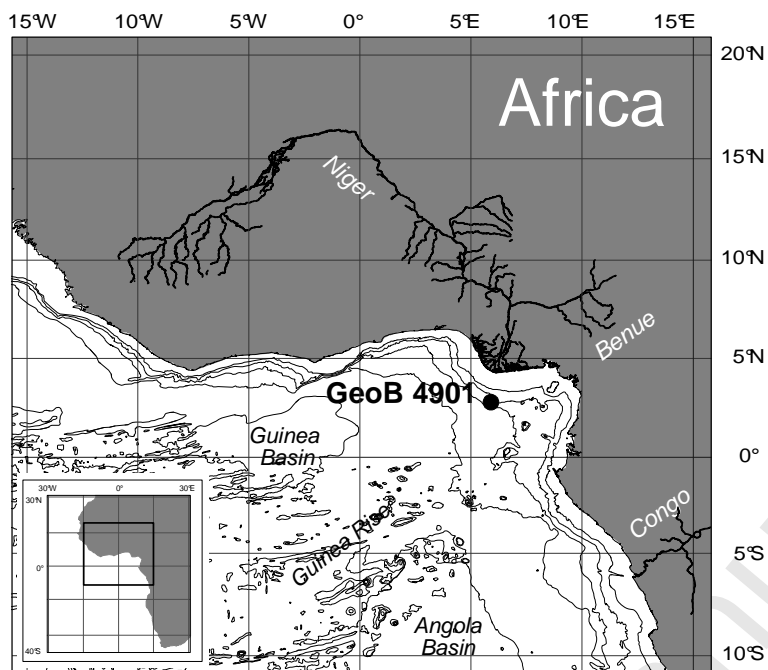
938 Table 3 Relative abundances of mineral components in the upper suboxic and lower anoxic
 939 magnetic extracts.

Component	Suboxic	Anoxic
Magnetite	18.9%	0%
Titanomagnetite	62.3%	5.4%
Hemoilmenite	16.9%	66.2%
Others	1.9%	28.4%

940

941 Table 4 Temperature-dependent values for hysteresis parameters saturation magnetization M_s , saturation remanence M_{rs} and coercive force B_c .

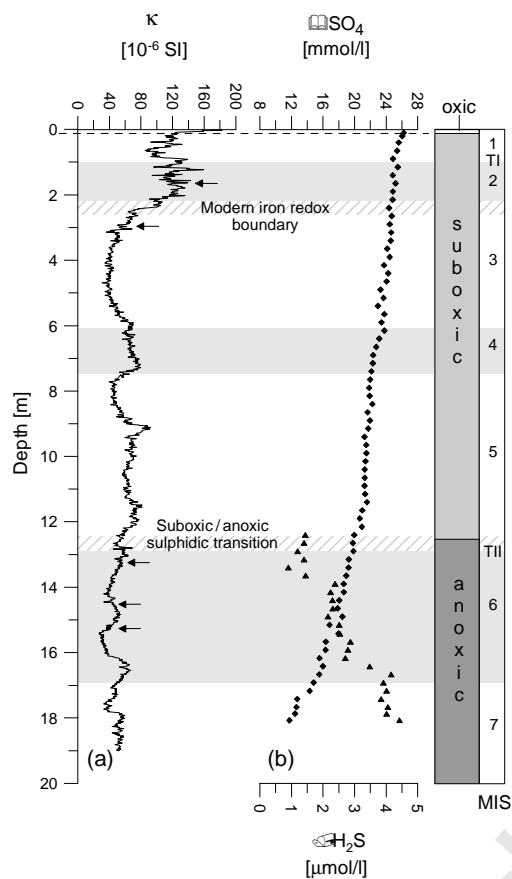
T [K]	1.65 m			2.95 m			13.25 m			14.55 m			15.25 m		
	M_s [10^{-6} Am 2]	M_{rs} [10^{-6} Am 2]	B_c [mT]	M_s [10^{-6} Am 2]	M_{rs} [10^{-6} Am 2]	B_c [mT]	M_s [10^{-6} Am 2]	M_{rs} [10^{-6} Am 2]	B_c [mT]	M_s [10^{-6} Am 2]	M_{rs} [10^{-6} Am 2]	B_c [mT]	M_s [10^{-6} Am 2]	M_{rs} [10^{-6} Am 2]	B_c [mT]
295	3.98	0.67	12.56	1.59	0.25	10.31	0.78	0.13	9.47	0.36	0.05	6.80	0.46	0.06	9.17
245	3.98	0.74	15.05	1.71	0.30	12.96	0.93	0.19	13.56	0.42	0.07	10.15	0.52	0.09	12.87
195	4.02	0.81	17.54	1.72	0.35	16.28	1.06	0.26	19.65	0.48	0.10	14.82	0.58	0.12	18.97
145	4.00	0.87	19.98	1.74	0.39	20.67	1.19	0.34	29.77	0.51	0.12	21.79	0.65	0.17	28.32
110	4.02	0.91	22.19	1.76	0.43	24.89	1.28	0.40	40.72	0.53	0.15	29.44	0.69	0.20	38.54
75	4.04	0.98	25.54	1.75	0.47	30.74	1.35	0.48	56.32	0.56	0.18	39.62	0.73	0.24	52.20
60	4.03	1.01	27.05	1.75	0.49	33.58	1.37	0.52	65.08	0.57	0.20	45.40	0.74	0.26	60.00
50	4.02	1.03	28.30	1.75	0.50	35.96	1.39	0.55	73.26	0.57	0.21	50.55	0.75	0.28	68.20
40	4.03	1.08	30.56	1.75	0.53	39.82	1.41	0.58	84.67	0.58	0.22	57.60	0.76	0.29	77.89
35	4.04	1.12	31.93	1.75	0.55	41.95	1.43	0.61	93.12	0.59	0.23	62.39	0.76	0.30	84.98
30	4.05	1.18	34.41	1.76	0.57	46.09	1.45	0.63	104.25	0.59	0.24	69.05	0.77	0.32	93.69
25	4.10	1.23	36.93	1.78	0.60	49.68	1.47	0.67	118.51	0.60	0.25	78.13	0.78	0.33	104.76
20	4.12	1.27	39.73	1.80	0.61	54.41	1.49	0.70	135.97	0.60	0.27	87.98	0.79	0.35	118.60
15	4.19	1.29	43.60	1.84	0.62	57.71	1.51	0.74	163.73	0.62	0.28	102.12	0.81	0.37	140.50
10	4.36	1.28	46.65	1.89	0.63	62.33	1.58	0.80	195.91	0.64	0.30	119.85	0.83	0.39	171.30
5	4.60	1.30	49.81	1.98	0.65	66.60	1.68	0.86	233.50	0.67	0.31	140.45	0.89	0.42	205.10



942

943

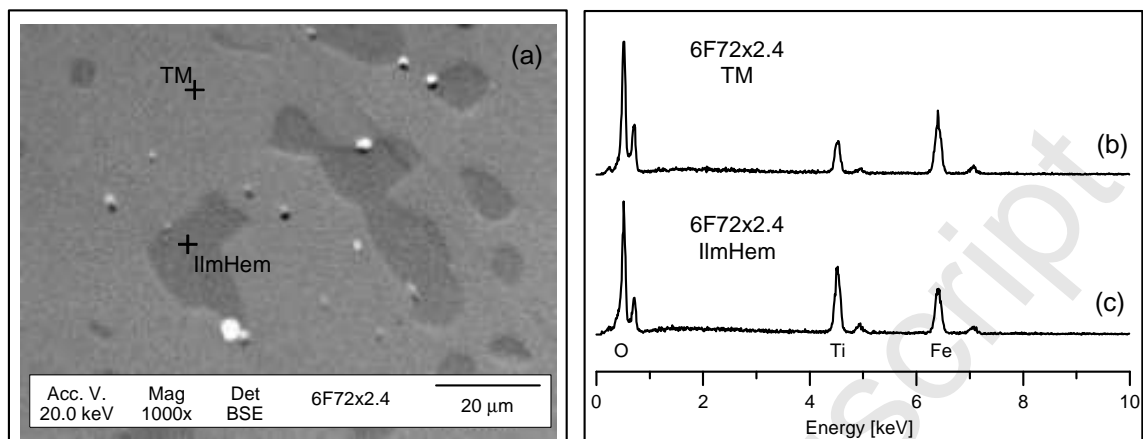
944 Fig. 1 Location of sediment coring site GeoB 4901 in 2184 m water depth on the
945 southeastern flank of Niger deep-sea fan ($02^{\circ}40.7'N / 06^{\circ}43.2'E$). Isobaths are shown at
946 1000 m intervals according to Intergovernmental Oceanographic Commission (1994).



947

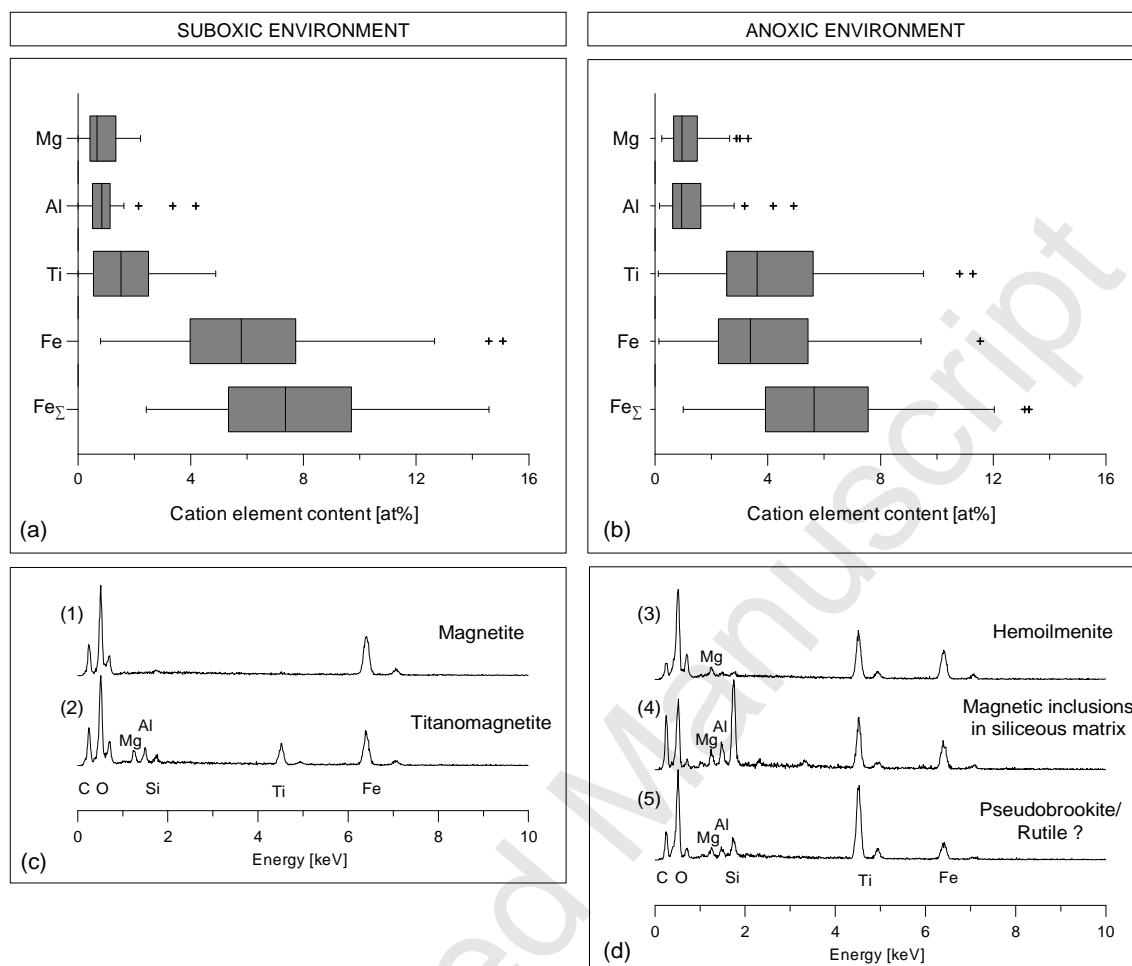
948 Fig. 2 (a) Depth profile of the volume specific bulk susceptibility κ delineating variations in
 949 the concentration of magnetic minerals. (b) Pore water chemistry at Site GeoB 4901 (Heuer,
 950 2003). All parameters are plotted against a linear depth scale and a non-linear age scale
 951 (Adegbie, 2001) including marine oxygen isotope stages (MIS) and terminations (T). Grey
 952 shading indicates cold periods. Horizontal hatched bars mark the modern iron redox boundary
 953 (~2.85 m) and the suboxic / sulfidic anoxic transition (~12.5 m). Arrows at the κ profile
 954 denote the horizons, where detailed magnetic analyses have been performed.

955



956

957 Fig. 3 (a) Backscattered electron micrograph of synthetic sample 6F72x2.4, light grey areas
958 correspond to TM63 (Fe-richer) and darker grey areas correspond to Ilm76Hem24 (Fe-
959 poorer). (b) EDS spectrum of the TM63 phase from the spot marked in (a). (c) EDS spectrum
960 of the Ilm76Hem24 phase from the spot marked in (a).



961

962 Fig. 4 Univariate box-and-whisker plots of the cation element content for the main elements
 963 Fe and Ti and minor contributions of Mg and Al of magnetic extracts from (a) the suboxic
 964 and (b) the anoxic sediments. Fe_{Σ} equals the sum of the three elements Fe, Mg and Al. The
 965 boxes represent the median values and the interquartile range, the whiskers mark the total data
 966 range. Symbols (+) display outlier samples from the respective data group. (c) and (d) show
 967 typical element spectra for particles representing the different Fe-Ti oxide phases detected in
 968 the two geochemical environments (for further explanations see text).

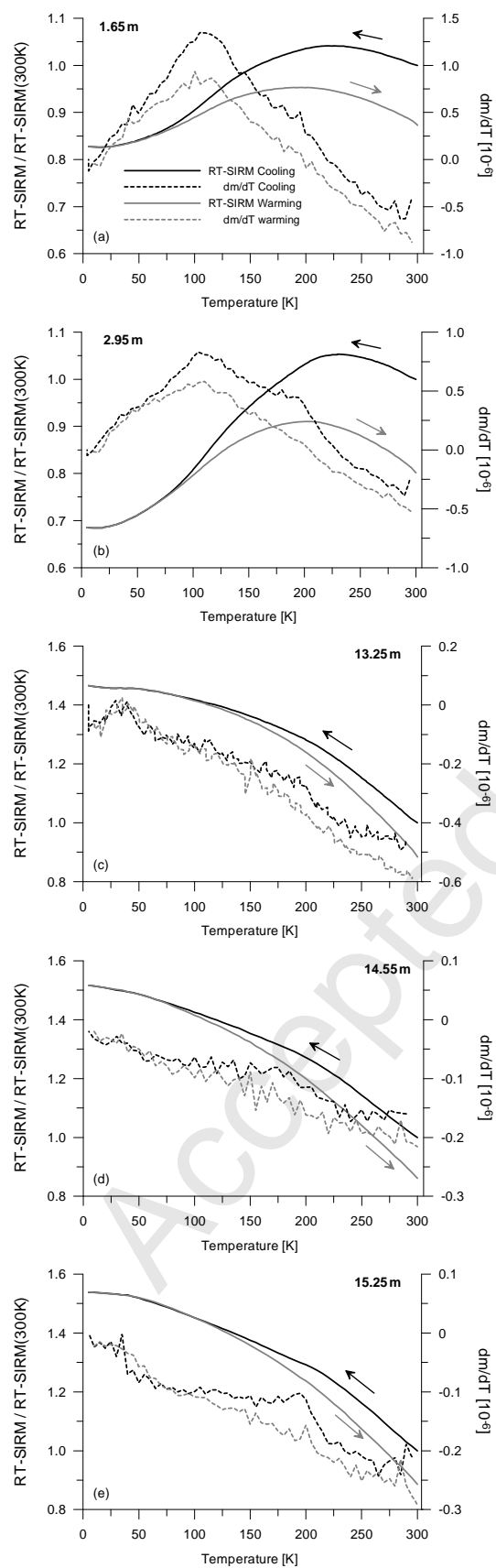
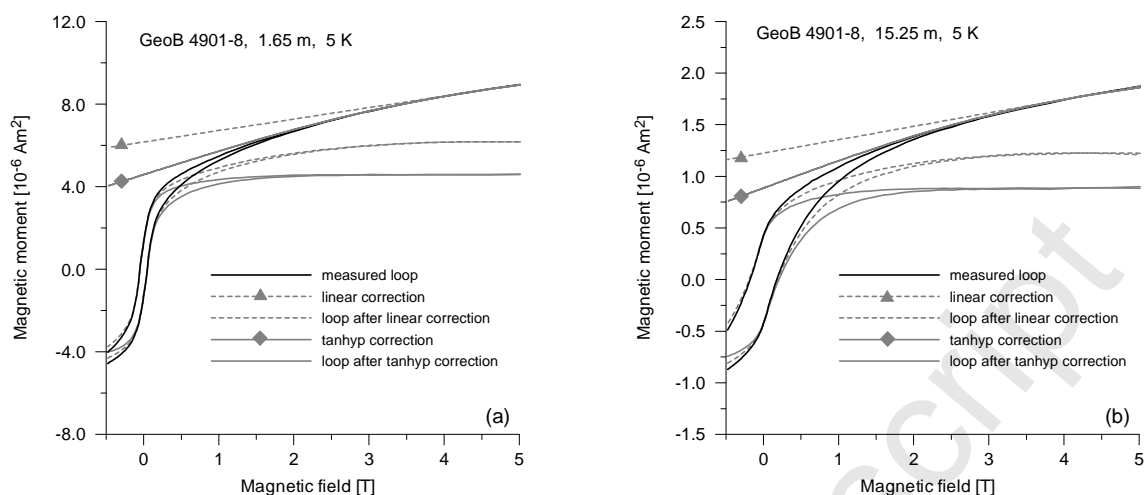


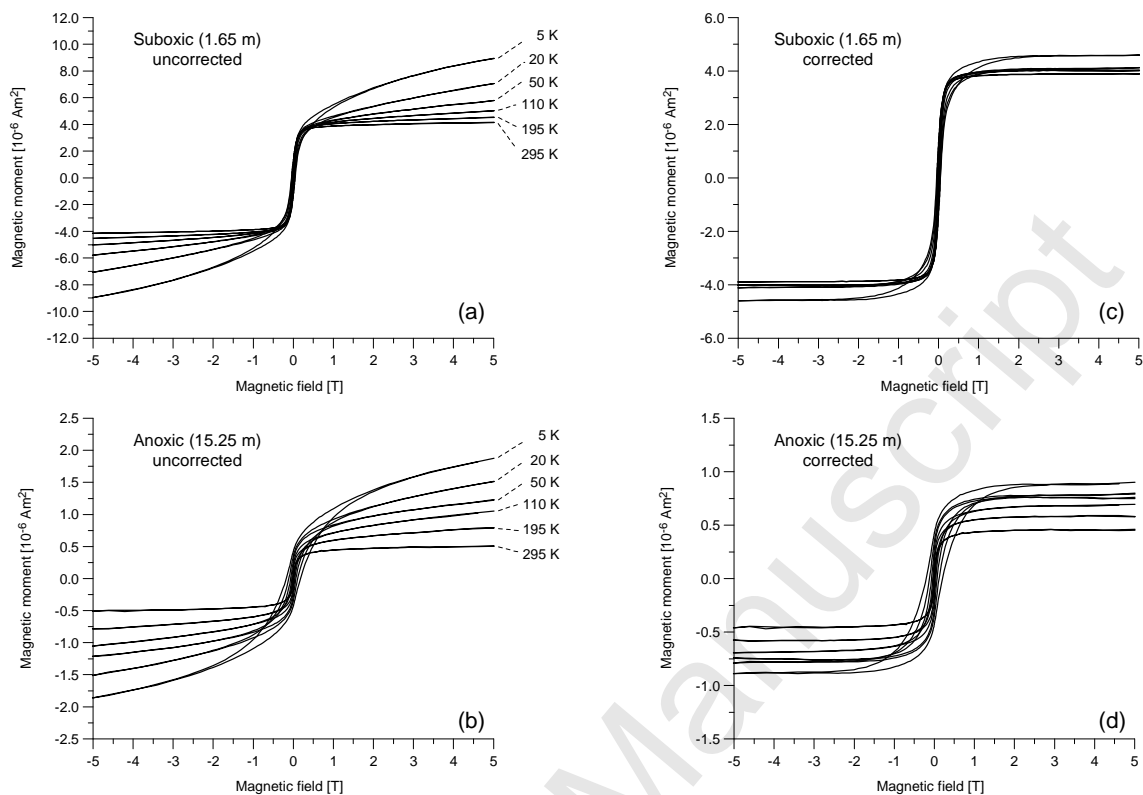
Fig. 5 Temperature variation of RT-SIRM during zero field cooling from 300 to 5 K (black solid line) and zero field warming back to 300 K (grey solid line). First derivative curves of the RT-SIRM curves are shown as dashed with the same color code.



970

971

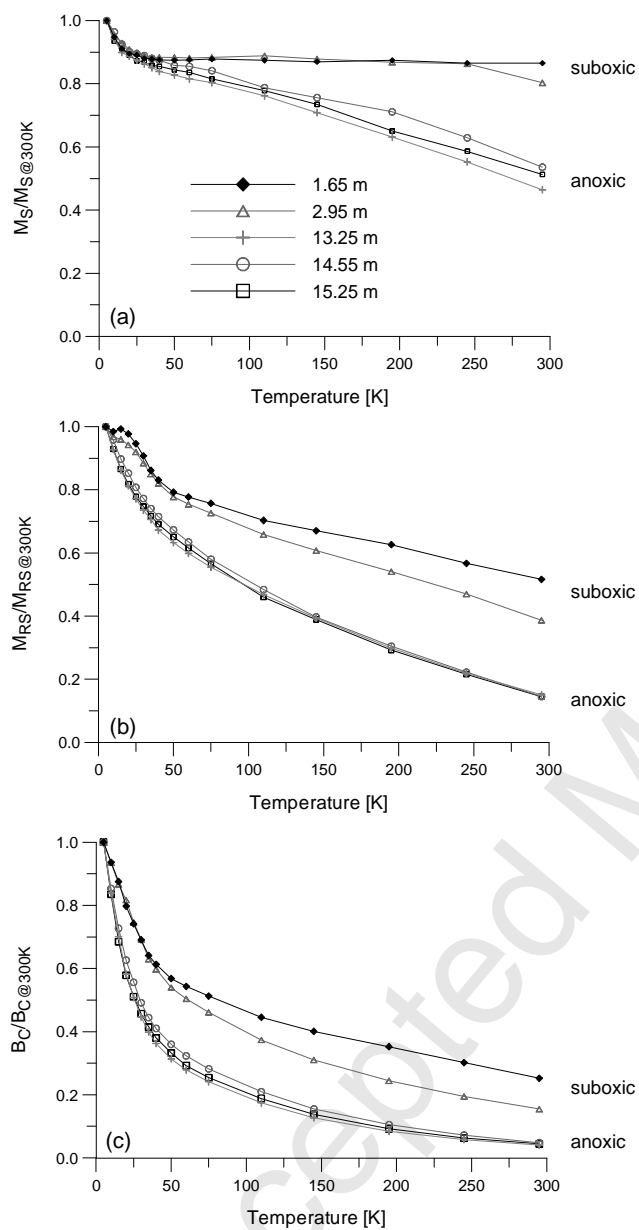
972 Fig. 6 Uncorrected (black solid line), linear slope corrected (grey solid line) and
 973 paramagnetic slope corrected (grey dashed line) hysteresis data shown for samples from (a)
 974 1.65 m and (b) 15.25 m core depth measured at 5 K. Filled triangles indicate the high field
 975 slopes determined by least squares fit of data measured between 4 and 5 T; filled diamonds
 976 depict the paramagnetic slopes derived from the equation $m(B,T) = a \cdot \tanh(B/b)$.



977

978

979 Fig. 7 Low-temperature evolution of hysteresis loops for magnetic extracts from samples of
 980 the upper suboxic (a, b) and lower anoxic (c, d) core sections. For the sake of clarity,
 981 hysteresis loops at six selected temperatures are shown, indicated by small numbers in the left
 982 side panel. Data shown on the left are uncorrected, data on the right are corrected for dia- and
 983 paramagnetic contributions.

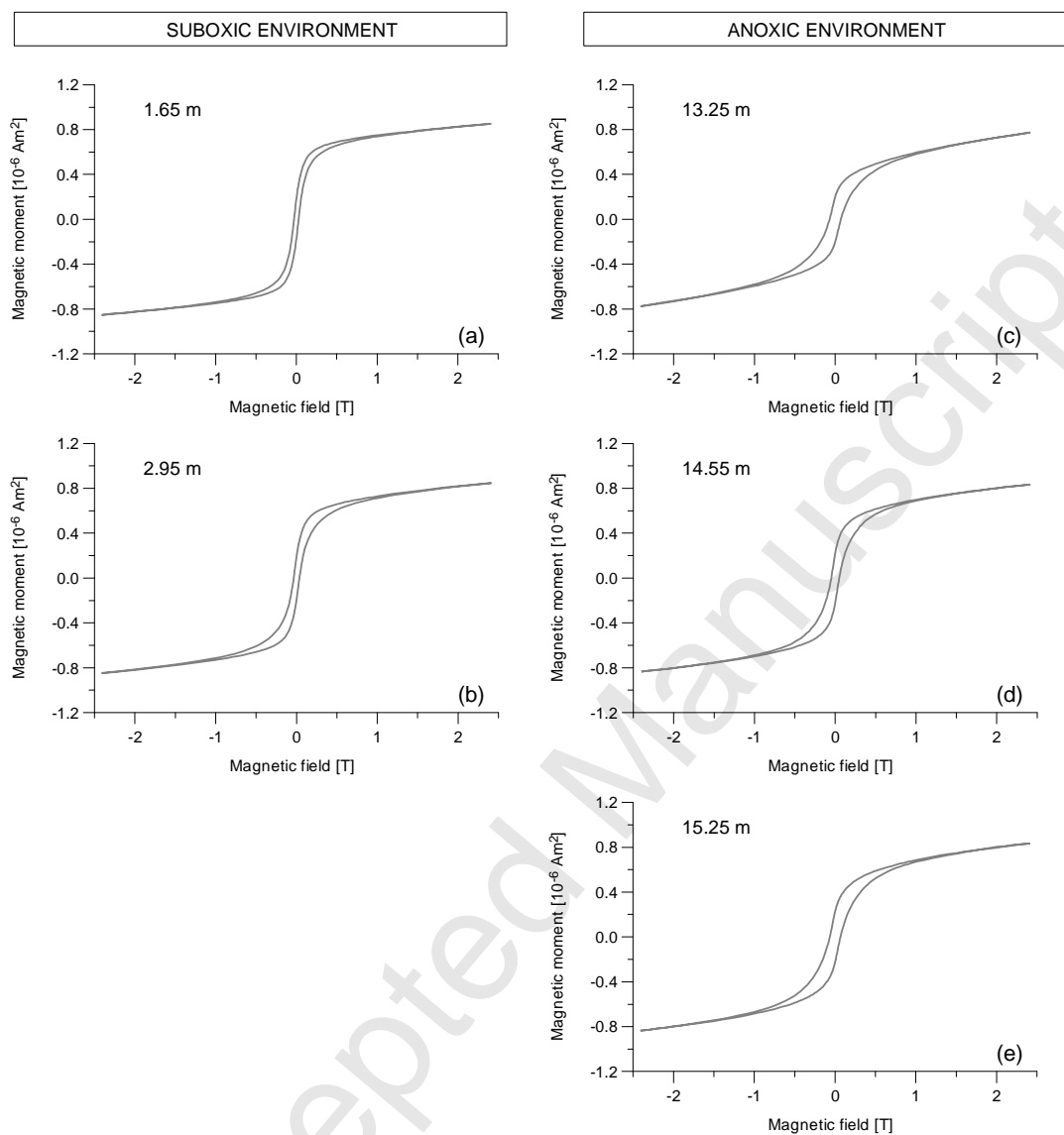


984

985

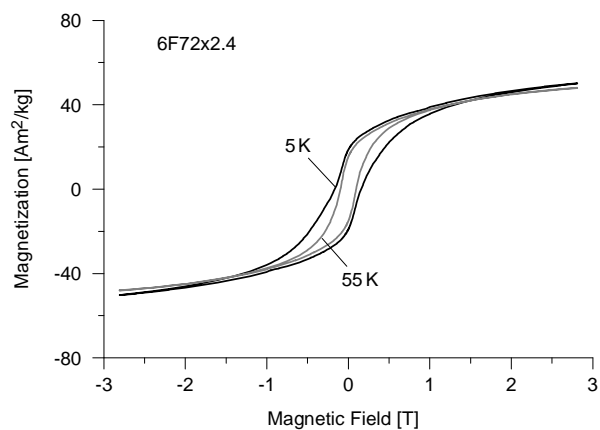
986 Fig. 8 Results of normalized hysteresis parameters: low-temperature dependence of (a)

987 saturation magnetization M_S , (b) saturation remanent magnetization M_{RS} , and (c) coercive988 field B_C .



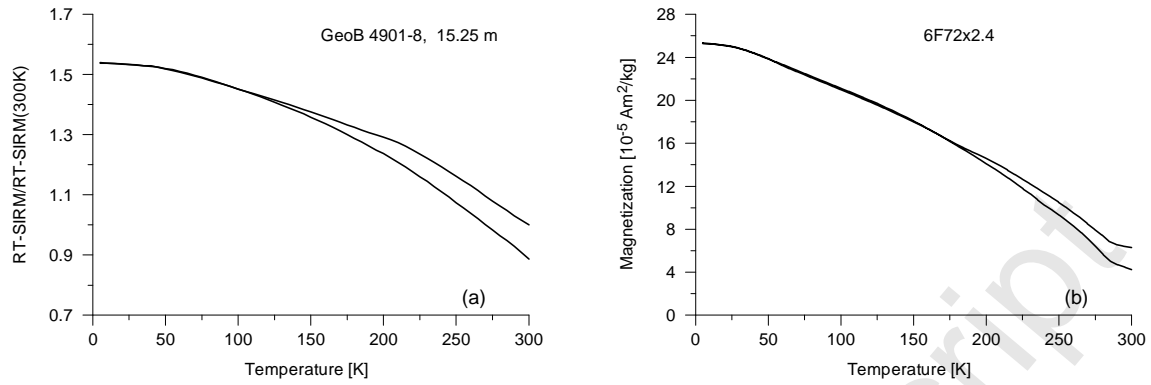
989

990 Fig. 9 Uncorrected hysteresis loops measured at 50 K; suboxic samples (a) and (b) show
991 slightly wasp-waisted characteristics, whereas anoxic samples (c) to (e) show a distinct wasp
992 waisted shape.



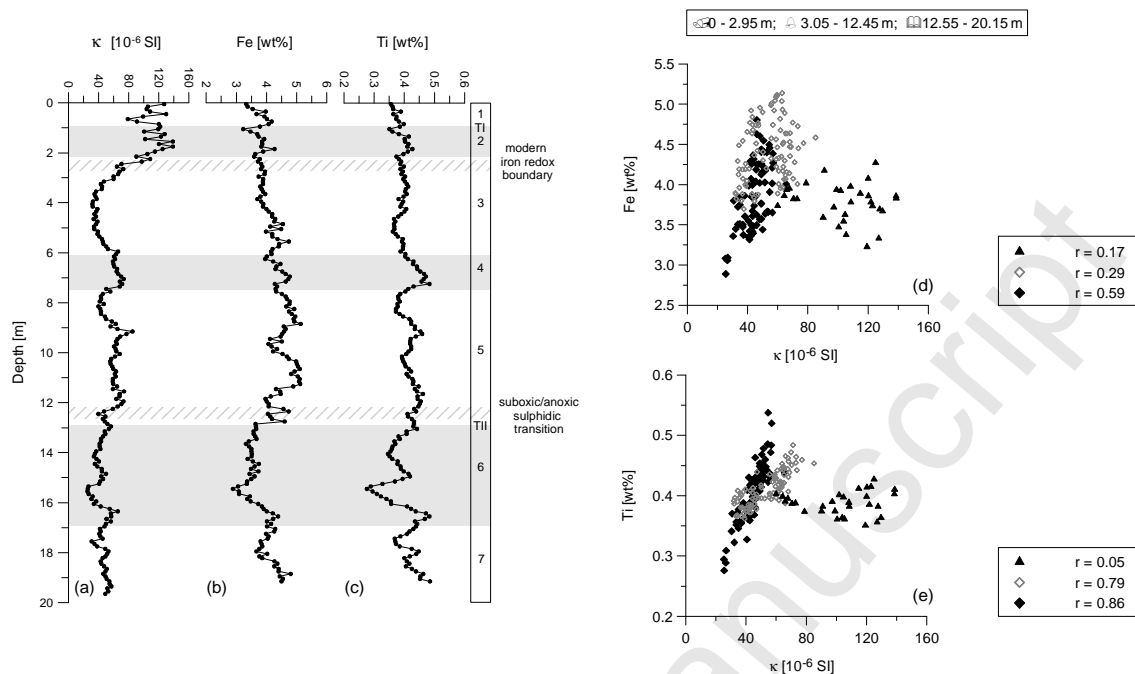
993

994 Fig. 10 Low-temperature hysteresis loops for synthetic sample 6F72x2.4 measured at 55 K
995 (black solid line) and 5 K (grey solid line), showing slightly (55 K) and pronounced (5 K)
996 wasp-waisted shapes (R. Engelmann et al., unpublished data).



997

998 Fig. 11 Low-temperature variation of RT-SIRM for (a) the magnetic extract from 15.25 m
999 depth and (b) the synthetic sample 6F72x2.4 (R. Engelmann et al., unpublished data).



1000

1001 Fig. 12 (left) Downcore profiles of (a) volume magnetic susceptibility κ and solid phase
 1002 concentrations of (b) Fe and (c) Ti (Zabel et al., 2001). All parameters are plotted on a linear
 1003 depth scale and a non-linear age scale (Adegbe, 2001) including marine oxygen isotope
 1004 stages (MIS) and terminations (TI, TII). Grey shading indicates cold periods. For further
 1005 details see also Figure 2.

1006 (right) Correlation of (d) κ vs. Fe-content, and (e) κ vs. Ti-content. Symbols indicate data
 1007 points for the upper three metres (black triangles), the depth interval from 3.0 m to 12.5 m
 1008 (open grey diamonds) and below 12.5 m (filled black diamonds). Pearson's correlation
 1009 coefficients r are given for the respective depth intervals.

1010